SAND 76-0005
Unlimited Release

COMPRESSION WAVE STUDIES IN BLAIR DOLOMITE

D. E. Grady, R. E. Hollenbach, K. W. Schuler, 5163
J. F. Callender, UNM

Prepared by Sandia Laboratories, Albuquerque, New Mexico 87115 and Livermore, California 94550 for the United States Energy Research and Development Administration under Contract AT (29-1)-789

February 1976

Sandia Laboratories

SF 2900 Q(7-73)

When printing a copy of any digitized SAND Report, you are required to update the markings to current standards.

Issued by Sandia Laboratories, operated for the United States Energy Research and Development Administration by Sandia Corporation.

NOTICE

This report was prepared as an account of work sponsored by the United States Government. Neither the United States nor the United States Energy Research and Development Administration, nor any of their employees, nor any of their contractors, subcontractors, or their employees, makes any warranty, express or implied, or assumes any legal liability or responsibility for the accuracy, completeness or usefulness of any information, apparatus, product or process disclosed, or represents that its use would not infringe privately owned rights.

Printed in the United States of America
Available from
National Technical Information Service
U. S. Department of Commerce
5285 Port Royal Road
Springfield, VA 22151
Price: Printed Copy $5.50; Microfiche $2.25

SAND 76-0005
Unlimited Distribution
Printed February 1976

COMPRESSION WAVE STUDIES IN BLAIR DOLOMITE

D. E. Grady, R. E. Hollenbach, K. W. Schuler
Shock Wave Phenomena Division, 5163
Sandia Laboratories
Albuquerque, New Mexico 87115

J. F. Callender
University of New Mexico
Albuquerque, New Mexico 87106

ABSTRACT

Dynamic compression wave studies have been conducted on Blair dolomite in the stress range of 0-7.0 GPa. Impact techniques were used to generate stress impulse input functions, and diffuse surface laser interferometry provided the dynamic instrumentation. Experimental particle velocity profiles obtained by this method were coupled with the conservation laws of mass and momentum to determine the stress-strain and stress-modulus constitutive properties of the material. Comparison between dynamic and quasistatic uniaxial stress-strain curves uncovered significant differences. Energy dissipated in a complete load and unload cycle differed by almost an order of magnitude and the longitudinal moduli differed by as much as a factor of two. Blair dolomite was observed to yield under dynamic loading at 2.5 GPa. Below 2.5 GPa the loading waves had a finite risetime and exhibited steady propagation. A finite linear viscoelastic constitutive model satisfactorily predicted the observed wave propagation. We speculate that dynamic properties of preexisting cracks provides a physical mechanism for both the rate dependent steady wave behavior and the difference between dynamic and quasistatic response.

I. INTRODUCTION

A need for constitutive relations to predict the response of rock and rock masses to transient dynamic loading has come from such critical problem areas as earth penetration, design and hardening of structures to explosive or earthquake induced ground shock effects, rapid excavation, and *in situ* preparation of coal, shale, mineral, or geothermal deposits. Considerable effort has been expended to develop constitutive models and provide an experimental data base. Problems remain, however, as verified by the frequent inadequacy of predictions.

There is a current trend toward increasing reliance exclusively on quasistatically generated stress-strain data as the data base for determining dynamic constitutive models. This trend is understandable since the experimental requirements using static triaxial facilities are somewhat easier to fulfill than the equivalent dynamic tests, and the flexibility of choosing the loading and unloading paths is an attractive feature not available in a rapid dynamic experiment. There is, however, a certain danger associated with this trend unless verification can be provided to show that such extrapolation of static models to dynamic events is legitimate. It has not been conclusively demonstrated that rate dependent properties of rock media will allow such extrapolation without severely compromising the predictions.

One aspect of the present study was to compare the static and dynamic properties of rock media. In Fig. 1 we compare uniaxial strain data obtained on Blair dolomite under conditions of static loading (Heard *et al.*[1]) and impact load (present work). This figure clearly illustrates the potential pitfalls which can occur. The data show that energy dissipated in a

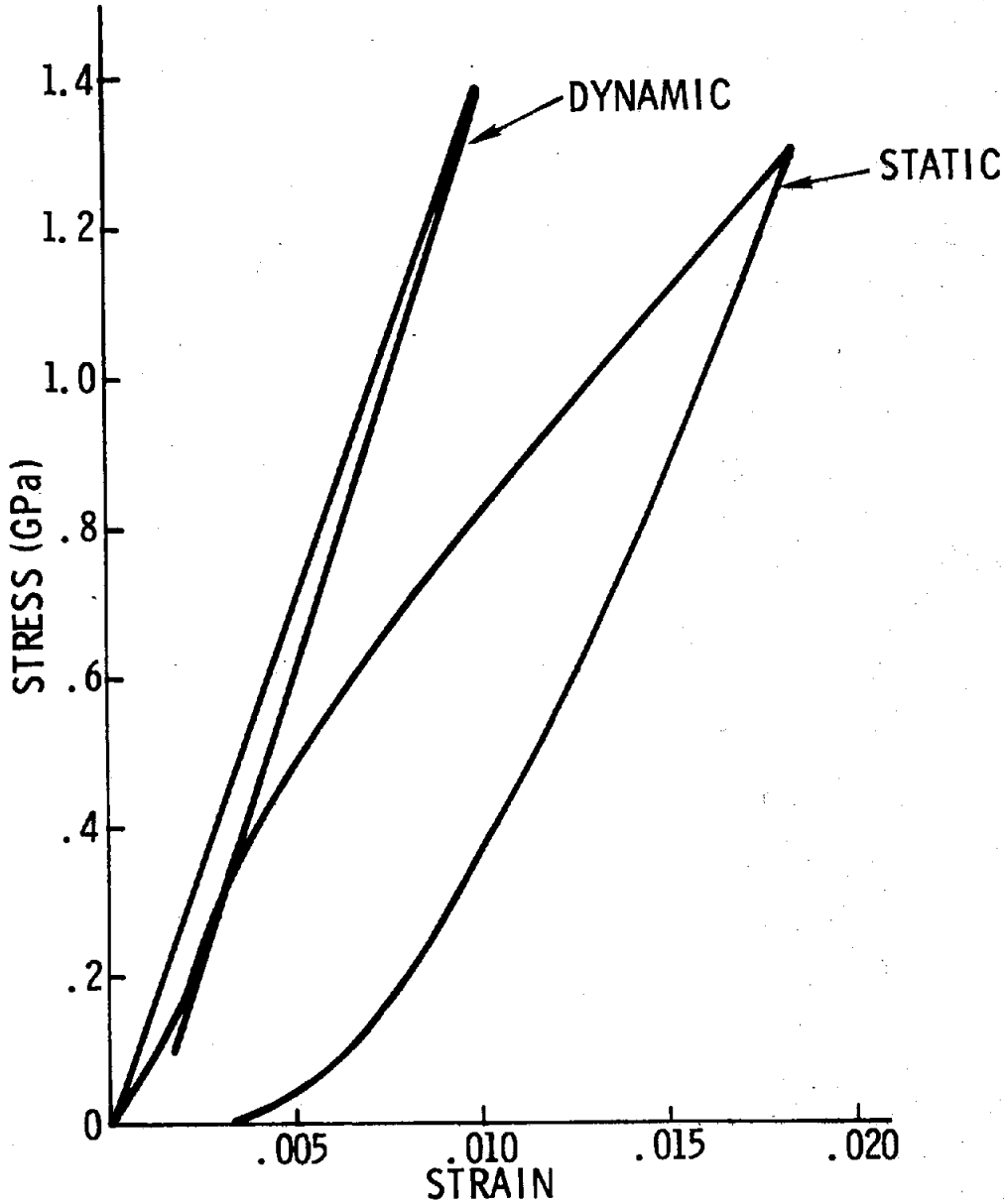

Fig. 1: UNIAXIAL STRAIN CURVES FOR BLAIR DOLOMITE.

The dynamic data was obtained in the present study with controlled plate impact techniques ($\dot{\epsilon} \approx 10^6$ sec^{-1}). The static data was obtained by Heard et al.[1] with triaxial compression facilities ($\dot{\epsilon} \approx 10^{-4}$ sec^{-1}).

complete load-unload cycle differ by approximately one order of magnitude and that material moduli differ by as much as 100 percent. It is easy to see that constitutive models based on the static data would fail totally in accurately predicting wave propagation in this material.

The purpose of this report is to summarize our findings on the transient dynamic mechanical properties of one rock, Blair dolomite. This work is one step in a systematic study designed to provide a firmer understanding of dynamic rock mechanics phenomenon and assist in the selection and development of adequate constitutive models appropriate for competent rock materials.

Controlled plate impact experiments were conducted to provide dynamic stress states in the range 0-7.0 GPa.* Impact conditions were specified so that the entire loading and unloading history of the dolomitic rock could be investigated. Diffuse surface laser interferometry recently developed by Barker and Hollenbach[2] provided dynamic instrumentation. This new technique does not have the severe optical reflectivity requirements of earlier systems, and it has made feasible the study of dynamic wave propagation in rock media with this accurate instrumentation capability. A particularly attractive feature is the ability to obtain fine detail in the unloading wave structure which has been difficult with other transducer techniques.

---

*In adherence to SI units we have adopted as the unit of pressure 1 GPA = 10^9 Pascals = 10^9 newtons/square meter = 10 kilobars.

II. EXPERIMENTAL PROCEDURES

One-dimensional plane waves were generated and subsequently measured in prepared samples of Blair dolomite. The experimental procedures which were used in the present study have been documented in detail in another report,[17] however, for completeness we will briefly summarize the important points.

The experimental methods which have been employed in this laboratory to investigate the dynamic mechanical properties of rock and soil media under conditions of plate impact are illustrated in Fig. 2. A 0.1 diameter light gas gun is used to impel flat-nosed aluminum projectiles at the target media. Projectiles are faced with thin plates of mechanically well characterized impact material which are backed with low impedance solid foam. Fused quartz and copper were the standard impact materials used in the present study. Impact on the target material provides a step input stress wave in the sample material followed by an unloading wave originating at the impact plate solid foam interface. Projectile velocities ranging from 0.01 to 1.0 mm/μs can be controlled within about 2 percent and impact planarity can be maintained within 0.3 or 0.4 milliradians. The projectile velocity is measured by offset pins to within 0.2 percent, and impact time at center of impact is measured to within about 10 ns using an offset impact fiducial pin and a planarity measurement with coplanar flush pins or a center-of-impact ribbon fiducial technique.*

On the back surface of the sample, a laser window material is mounted. Although fused quartz, plexiglas, and sapphire have been calibrated for laser operation, only fused quartz has been used in the current study of

*Details concerning the Sandia gas gun operation and measurement techniques are reported in reference 7. The last impact time technique mentioned is new and will be documented by us in a later report.

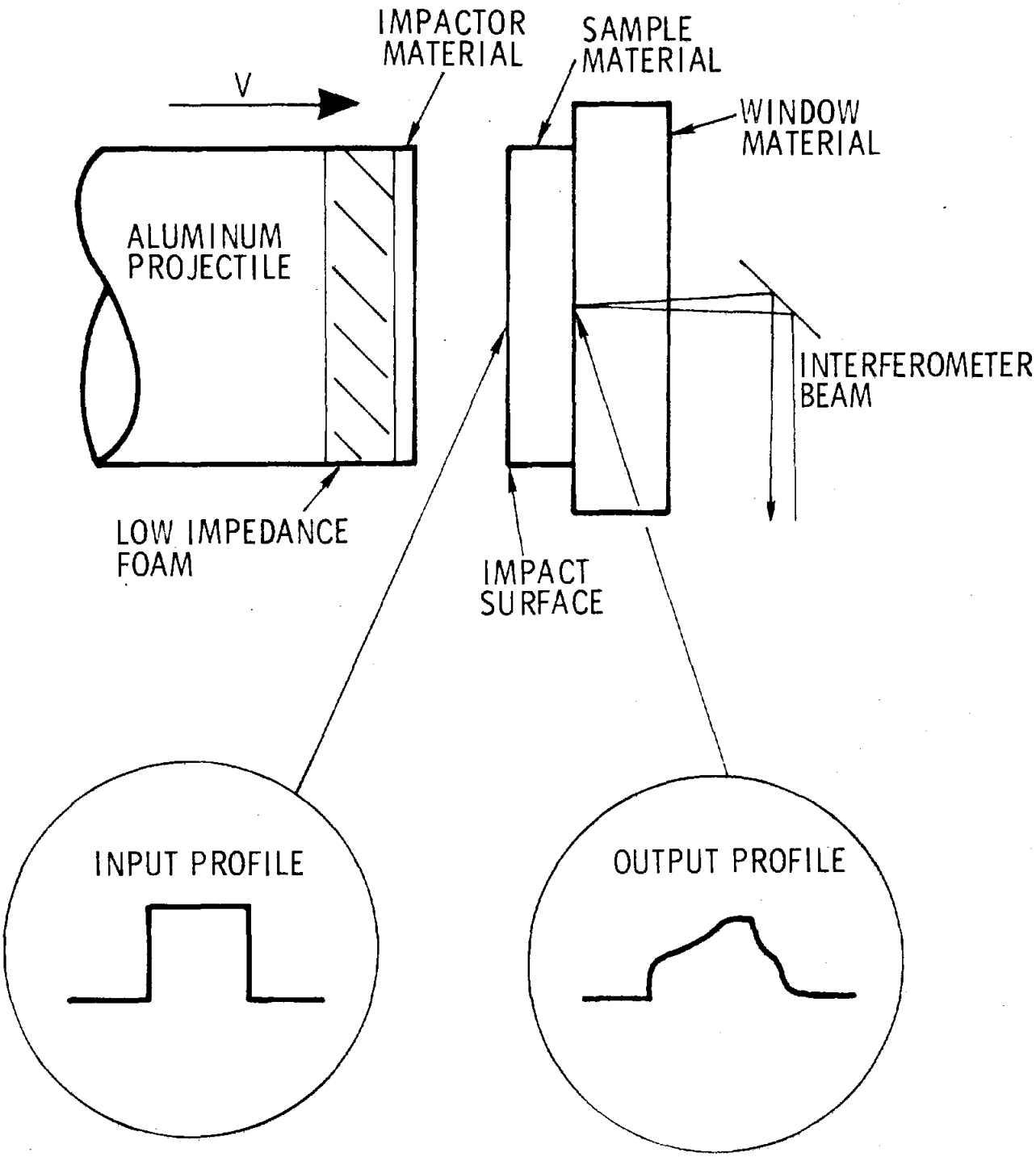

Fig. 2: IMPACT PROJECTILE, TARGET SYSTEM, AND INSTRUMENTATION.

Also illustrated is the input stress pulse and a representative output pulse.

rock properties. The window material surface in intimate contact with the sample surface is first vapor deposited with silver to provide a diffusely reflecting surface. Upon arrival of the stress wave at the sample-window interface, material velocity is continuously and accurately recorded through the complete history of loading and unloading with the diffuse surface velocity interferometer (VISAR).[2]

A series of tests on one rock material consists of selecting a number of impact amplitudes within the stress range of interest and conduct several experiments at each impact amplitude. Sample thickness at a fixed impact amplitude will be varied over the several experiments, usually ranging between 5 and 25 mm. By this procedure we can determine the evolution of the square wave input into the material which will be established by the particular constitutive properties of the rock under test.

III. MATERIAL CHARACTERIZATION

The dolomite selected for investigation in this work has received considerable attention in earlier static[1] and shock wave work.[3,4] Blair dolomite is a fairly homogeneous, fine-grain, equigranular dolomite [> 98 percent $CaMg(CO_3)_2$] obtained from Martinsburg, West Virginia. The measured dry density is 2.84 Mg/m^3, and the calculated porosity is 0.9 percent based on a crystal density of 2.866 Mg/m^3.* Petrographic analysis of one sample revealed a dolomitic, micritic limestone containing about 10 percent large (1.0-3.5 mm) dolomite crystals in a fine-grained (0.01-0.02 mm) micritic matrix. Large crystals show local fracturing and are commonly twinned; the matrix is generally unfractured, and is defined by optically discontinuous, equidimensional carbonate grains with local rhombohedral cleavage. Fractures and grain boundaries are sharply defined; grain boundaries are locally sutered and may be lined with organic material. Fracturing is relatively rare in the undeformed dolomite, and no preferred fabric is demonstrated.

Cylindrical samples 75 mm in diameter, ranging from 5 to 25 mm in thickness were prepared from a core of the dolomite. The material bedding plane was oriented perpendicular to the axis of shock propagation. Impact and recording faces of the samples were lapped. Both longitudinal and shear ultrasonic velocities were measured on all samples. The values obtained were C_l = 6.83 km/s and C_s = 4.03 km/s at a frequency of 2.25 Mhz. In several samples, fairly major crack systems were identified by reduced wave velocity and increased attenuation. These samples were not included with those that were shock-loaded.

---

*The sample of Blair dolomite used in the present work was kindly provided by Dr. W. J. Murri of Stanford Research Institute, Menlo Park, California.

†Ultrasonic velocities were provided by Larry Kent of Sandia Laboratories.

IV. EXPERIMENTAL DATA AND ANALYSIS

A total of 13 impact experiments were successfully completed on Blair dolomite. Experiments were performed at five impact velocities and two or more impact thicknesses were studied at each impact velocity level. A description of each impact experiment is provided in Table 1. Experimental data for each shot consists of oscilloscope traces of the two 90° out of phase VISAR photomultiplier outputs which contain the sample-window material interface motion history. An impact time of arrival fiducial is also provided on the same photomultiplier records.[7] The oscilloscope traces of the VISAR data are reduced to digital information on a telereader system and stored on computer disc. The digital VISAR data are reduced to particle velocity profiles of the sample-window interface history with a PDP-10 system user interaction computer program.[5]

Velocity profiles corresponding to the same impact velocity level are then scaled to correct for slight differences in impact velocity and impactor thickness. Since the window material is never an exact impedance match for the test material, a region of wave interaction is created in the test material near the sample-window interface and the measured interface velocity profile is a distorted version of the input profile in the specimen. The extent of distortion depends on the difference in the constitutive properties of the window material and the unknown constitutive properties of the sample material. A user interaction computer program has been developed which corrects the velocity profiles for impedance mismatch at the sample-window interface and provides the loading and unloading stress-strain, stress-particle velocity and longitudinal moduli of the sample material. This impedance correction and analysis routine is discussed in more detail elsewhere.[18]

TABLE I

DESCRIPTION OF IMPACT EXPERIMENT

Shot No.	Series No.	Impact Velocity km/s	Impact Material	Impactor Thickness (mm)	Sample Thickness (mm)	Window* Thickness (mm)
DS 105	1	.0778	FQ*	1.544	15.100	19.1
DS 106	1	.0774	"	1.524	20.163	25.4
DS 107	2	0.184	"	1.516	10.069	19.1
DS 108	2	0.184	"	1.638	15.080	19.1
DS 109	2	0.180	"	1.631	20.094	25.4
DS 101	3	0.351	"	1.560	8.0137	19.1
DS 102	3	0 350	"	2.510	13.025	25.4
DS 110	3	0.343	"	1 453	20.157	25.4
DS 103	4	0.618	"	1.544	8.026	19.1
DS 112	4	0.606	"	1.491	14.080	19.1
DS 113	5	0.569	Cu†	1.610	10.023	19.1
DS 114	5	0.571	"	1.577	14.943	19.1
DS 115	5	0.575	"	1.588	20.152	25.4

*Fused Quartz, Dynasil - 1000

†OFHC Copper

The experimental data will be presented in this section in the following order: First, the initial arrival transit time data for all experiments will be presented and discussed. Secondly, the experimental profiles and resulting constitutive properties for each impact velocity level will be presented in order. Each impact level will be identified by the series number given in Table 1. Lastly, the composite stress-strain, stress-particle velocity and longitudinal moduli results will be presented for all of the data.

First Arrival Velocity

The velocity corresponding to first arrival of the particle velocity wave profile was calculated from the transit time at impact to first break-away observed on the velocity interferometer record. The resulting velocities obtained in the present series of experiments are shown in Fig. 3. One data point is obtained per impact experiment.

In the figure, first arrival velocity is plotted as a function of the peak particle velocity recorded. The longitudinal ultrasonic velocity measured in this laboratory is also shown. Approximately 2 percent scatter was realized in the present set of experiments and the smooth curve provides a best fit to the first arrival velocity data. In further analysis of the experimental data, wave profiles were aligned in time according to the smoothed first arrival velocity data. Discussion of the trend observed in the initial arrival velocity will be deferred to a later section.

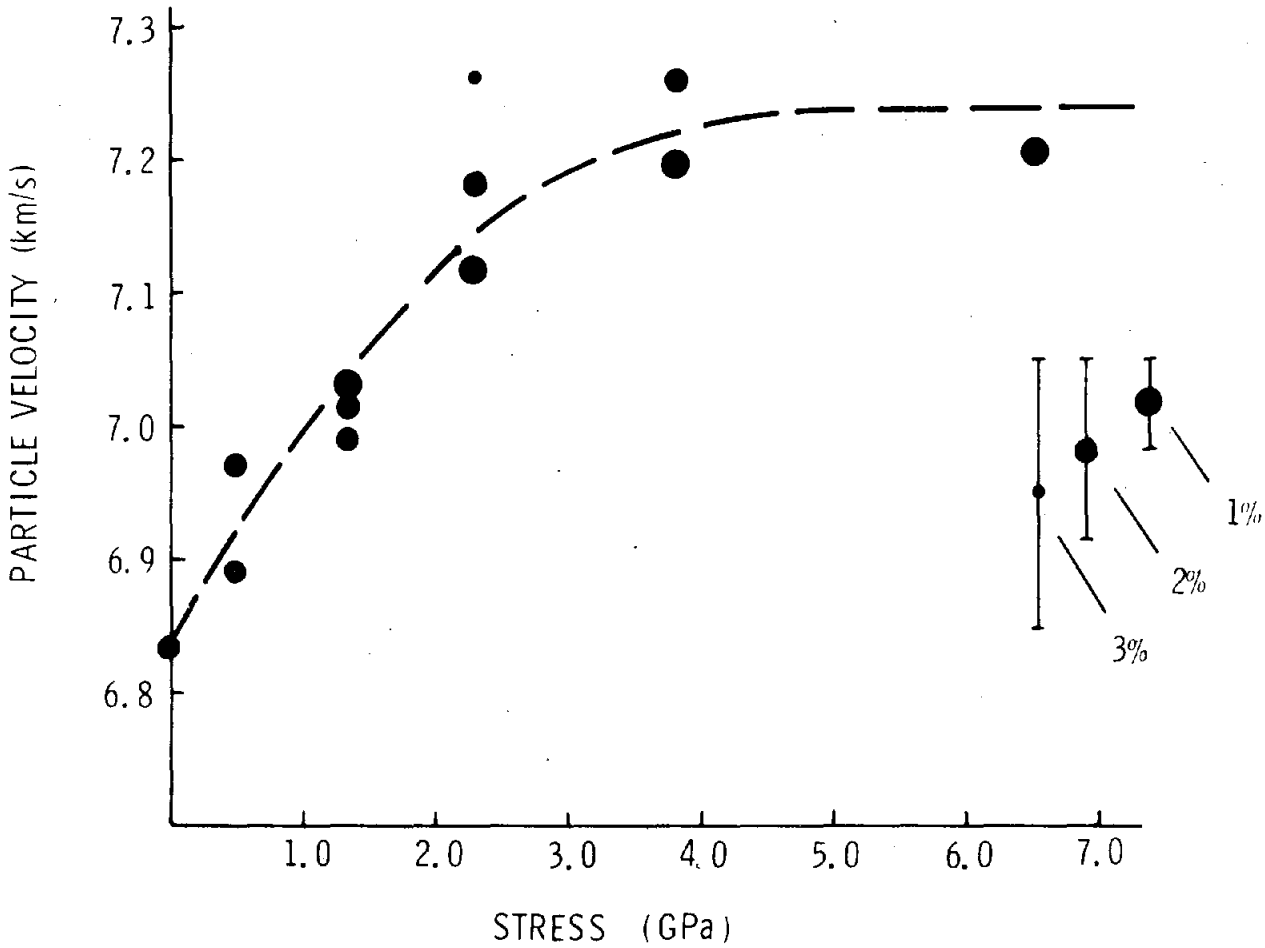

Fig. 3: FIRST ARRIVAL VELOCITY IN BLAIR DOLOMITE.

The abcissa is the peak stress achieved in the impact experiment. The approximate maximum error in individual experiments is indicated by the size of the symbol used.

Series 1 Data

At the lowest projectile impact velocity of 0.0776 mm/μs (255 ft/s) two tests were successfully completed. The sample thicknesses were approximately 15 mm and 20 mm (see Table I). In Fig. 4a the particle velocity profiles uncorrected for impedance differences between the fused quartz and the dolomite are displayed. In obtaining these final profiles the original profiles as determined directly from the VISAR records of the sample-window interface velocity are scaled to account for slight differences in impact velocity (Table 1) and the unloading wave adjusted for slight differences in impactor thickness (Table 1). The resulting profiles were then corrected for impedance differences as previously discussed.

Several traits in the profiles shown in Fig. 4a should be noted. The loading wave showed sharp shock characteristics to a velocity level of 0.0143 mm/μs. At this point there is a break after which the profile rises more gradually to a peak level over a period of about 0.2 μs. The loading profiles appeared to exhibit steady state or close to steady state wave propagation. In Fig. 5 the profiles have been normalized with respect to the transit time to illustrate the steady wave nature.

The detail observed in the unloading wave is not a property of the dolomite. During construction, epoxy was used to adhere the fused quartz impactor material to foam on the projectiles. The epoxy layer was somewhat thicker than is desirable, and produced the observed steps in the unloading wave. Only the initial portion of the unloading wave (breakaway and unloading down to the step) is accurate. Later tests benefited from the discovery of this problem, and the quality of the remaining unloading data was improved.

In Fig. 4 the stress-strain and stress-particle velocity curves and the wave velocity dependence on stress for both loading and unloading are shown. An estimate was made to correct the unloading wave for the small epoxy layer. There is an indication of a deviation from perfect elastic response by the slight hysteresis in the stress-strain curve.

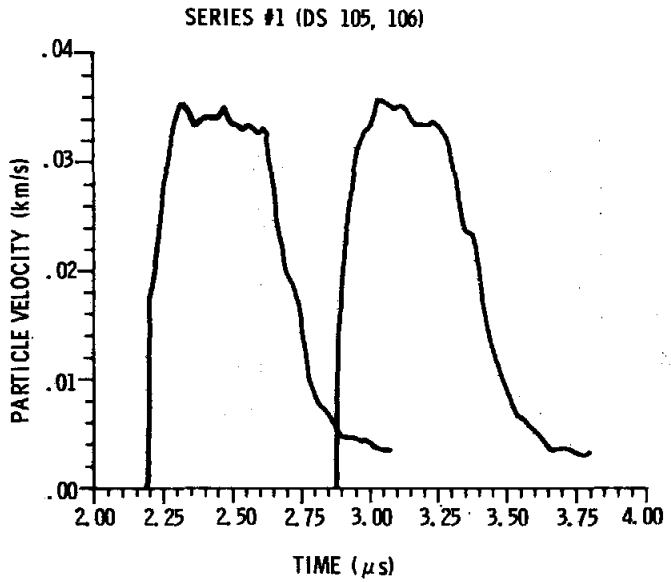

4a

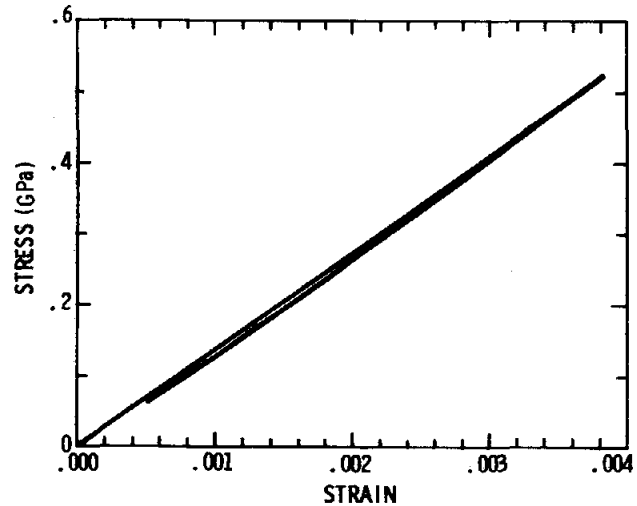

4b

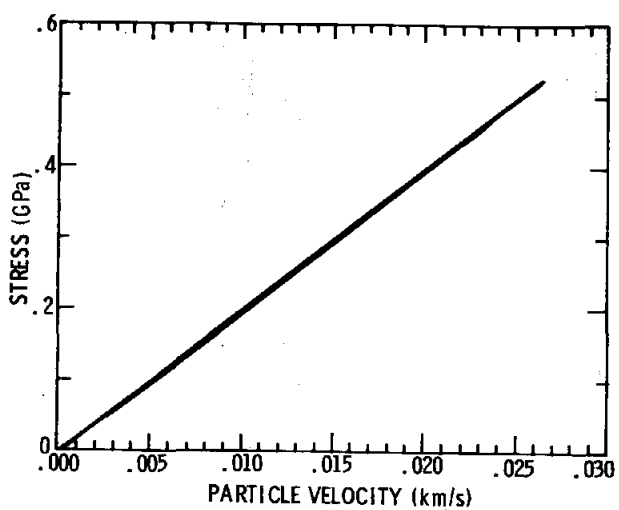

4c

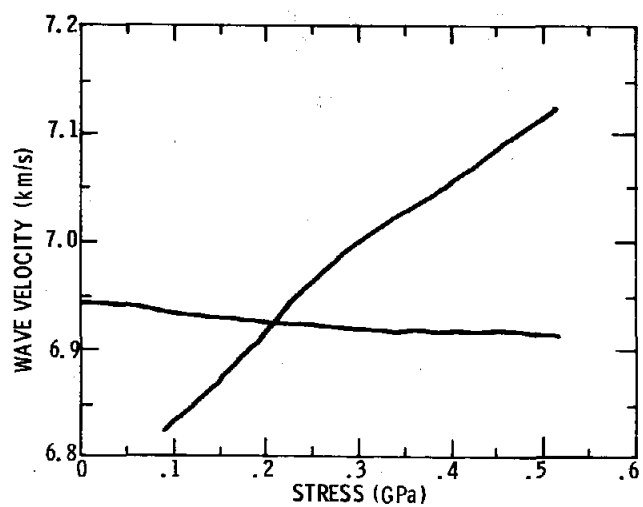

4d

Fig. 4: WAVE PROFILES AND CONSTITUTIVE PROPERTIES FOR SERIES 1 TESTS.

In Fig. 4-d the curve originating from zero stress corresponds to loading; the dispersive curve corresponds to unloading.

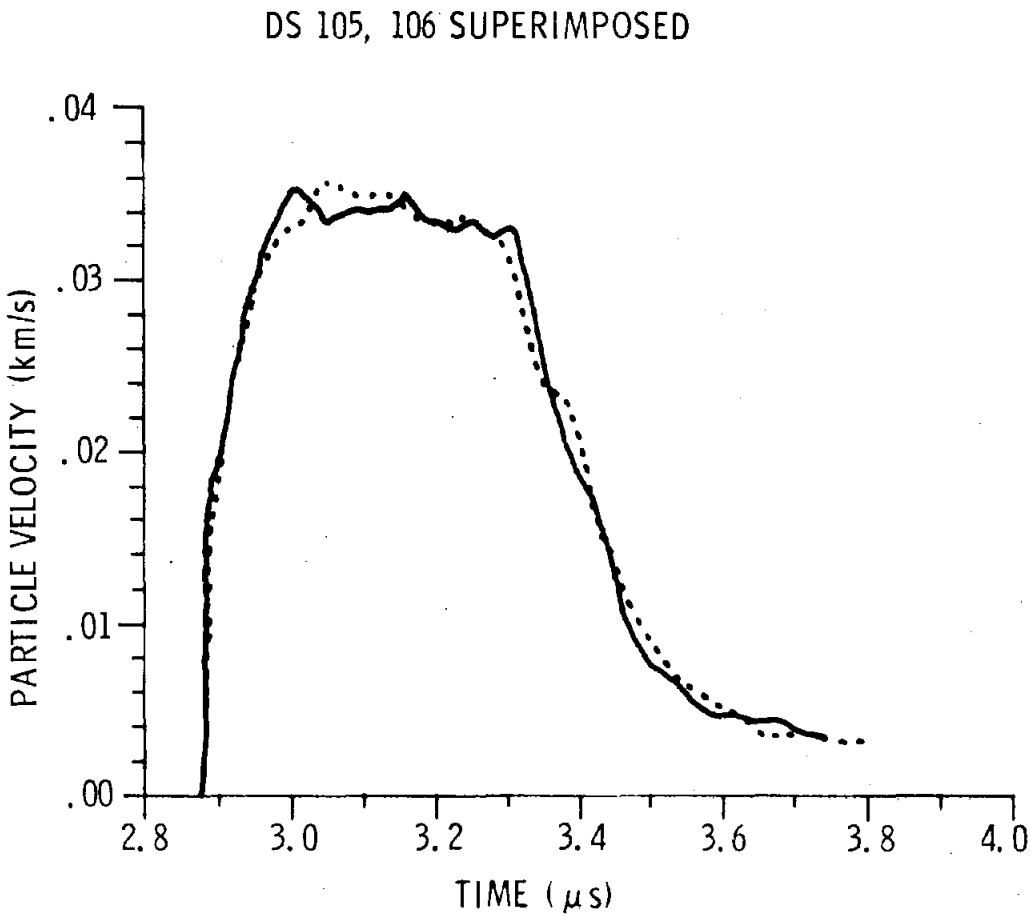

Fig. 5: SUPERIMPOSED SERIES 1 PROFILES.

The profiles were normalized in time to illustrate the loading steady wave propagation.

Series 2 Data

Projectile impact velocity for this series was 0.184 mm/μs (604 ft/sec) and three impact tests with sample thickness of approximately 10, 15, and 20 mm were successfully completed. The wave profiles are displayed in Fig. 6. As in Series 1, there was a sharp shock followed by a gradual rise over about 0.2 μs to the peak velocity level. The break as observed on the VISAR fringe records occurred at 0.037 mm/μs.

Again, steady wave propagation was noted for the loading wave profile over the approximately 10 mm propagation distance. In Series 2 the unloading wave is dispersive and significantly faster than the loading velocity. Hysteresis is somewhat more significant than in the Series 1 tests. These details can be seen in the stress-strain, stress-particle velocity and wave velocity curves shown in Fig. 6.

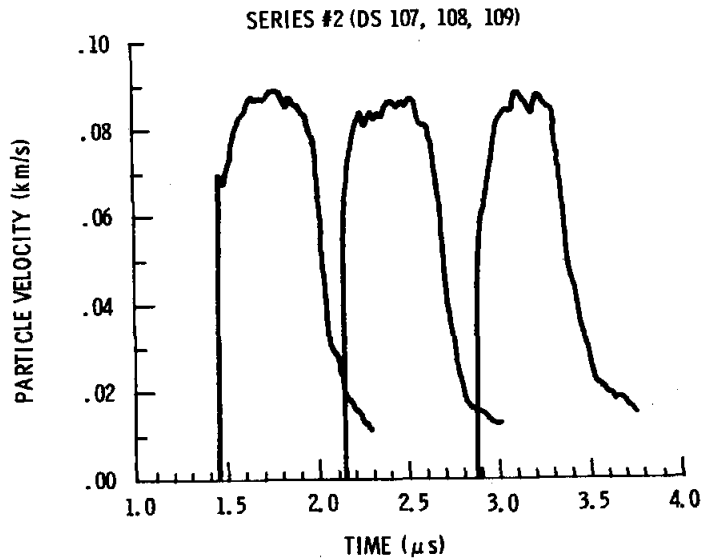

6a

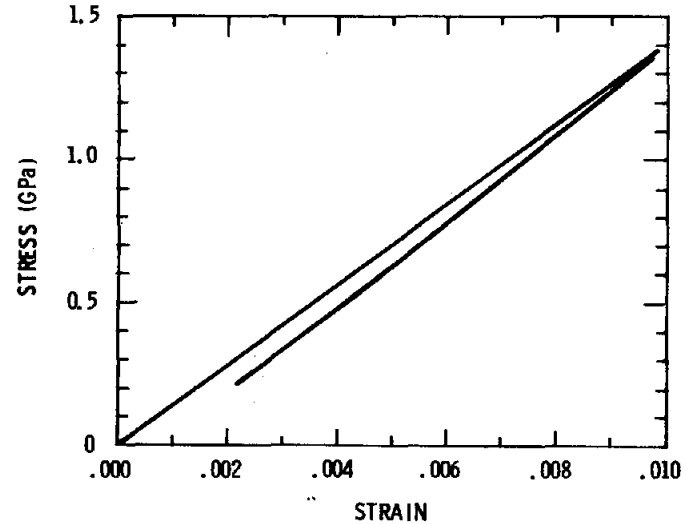

6b

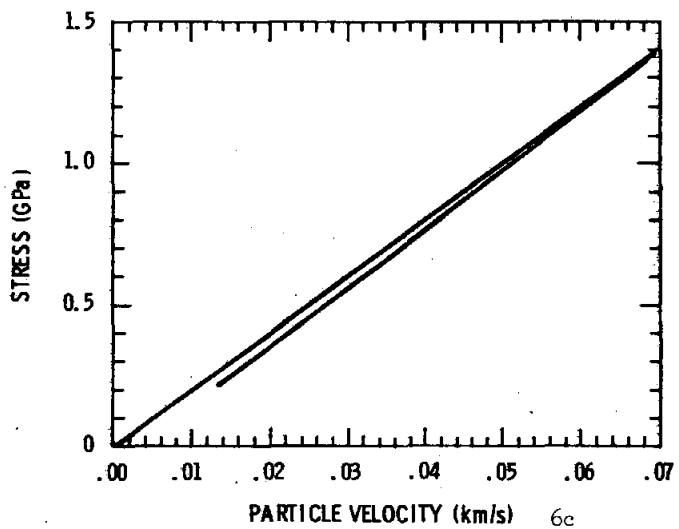

6c

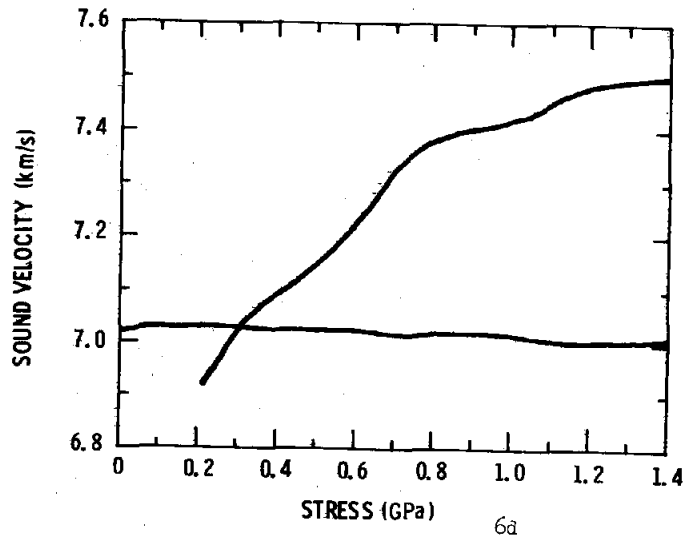

6d

Fig. 6: WAVE PROFILES AND CONSTITUTIVE PROPERTIES FOR SERIES 2 TESTS.

Series 3 Data

Impact velocity for Series 3 was 0.35 mm/μs (1148 ft/s). Three tests at sample thicknesses of approximately 8, 13, and 20 mm were completed. Particle velocity profiles are shown in Fig. 7. Although a peak particle velocity of approximately 0.15 mm/μs which corresponds to a peak stress of nearly 25 kilobars was attained, there is no clear indication that these profiles differ significantly in character from those obtained in Series 1 and Series 2. There is a sharp shock to a break of 0.087 mm/μs followed by a gradual rise to the peak velocity level. The loading wave propagation again appeared to be steady wave propagation. A faster dispersive unloading wave was observed. The plotted data in Fig. 7 show linear loading and slightly hysteretic unloading.

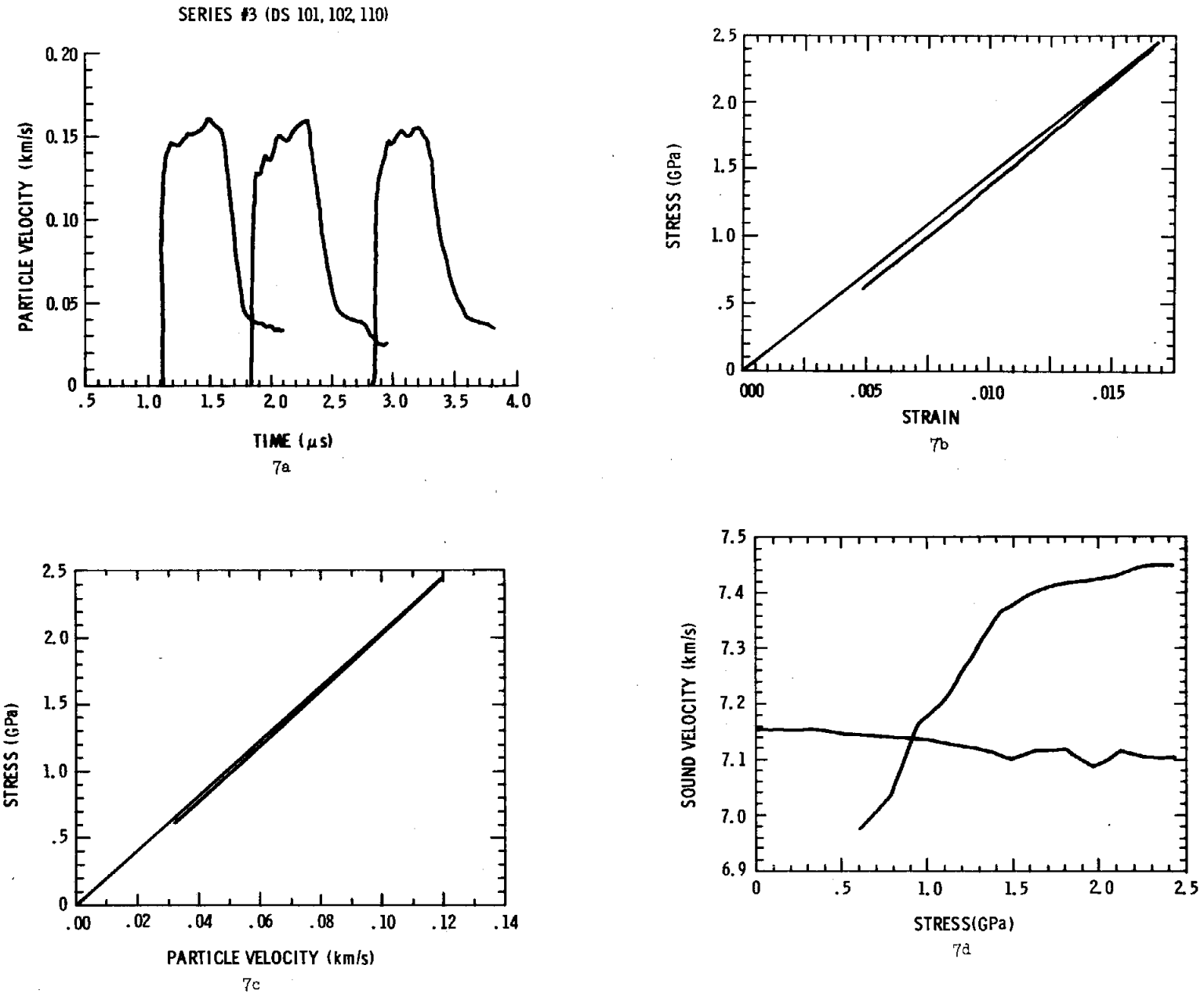

Fig. 7: WAVE PROFILES AND CONSTITUTIVE PROPERTIES FOR SERIES 3 TESTS.

Series 4 Data

Impact velocity for this series was 0.61 mm/μs (2000 ft/s) and two tests with sample thicknesses of 8 and 14 mm were successfully completed. Profiles are displayed in Fig. 8. The series 4 profiles show the first deviation from the propagation characteristics displayed by the first three series. At a velocity level of 0.15 mm/μs (corresponding to about 2.5 GPa) which is about the point of the profile break in Fig. 8, there is also a change in the loading wave velocity behavior. Above this level the wave is dispersive as is verified by the significant reduction in loading wave propagation velocity. The steady loading wave character displayed in the earlier series is no longer observed.

The stress-strain, stress-particle velocity, and wave velocity data are given in Fig. 8. The stress-strain character now shows some curvature on loading and the hysteresis is more significant. The wave velocity-stress plot clearly illustrates the reduction in velocity above about 2.5 GPa.

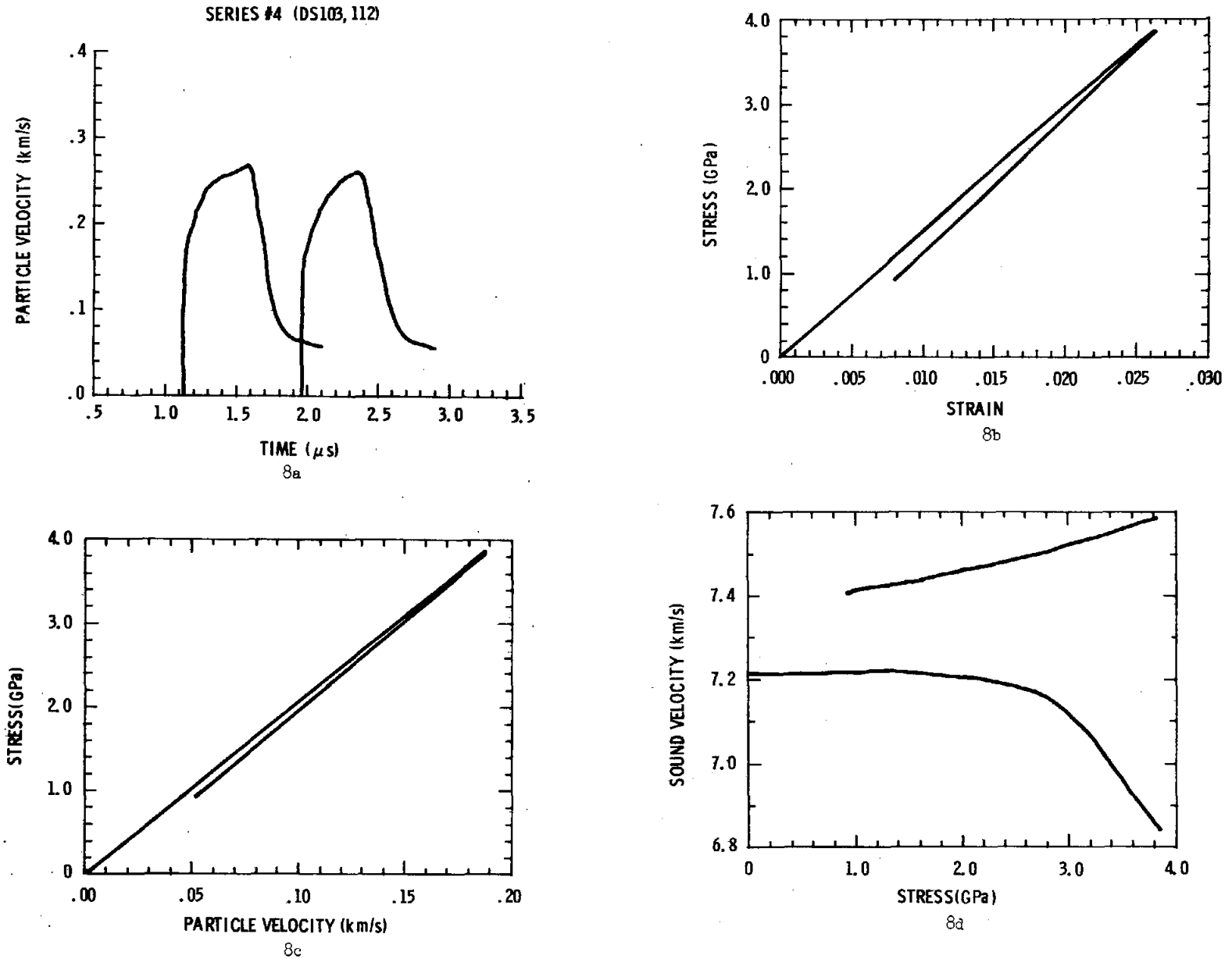

Fig. 8: WAVE PROFILES AND CONSTITUTIVE PROPERTIES FOR SERIES 4 TESTS.

Series 5 Data

Impact velocity for the final series was 0.57 mm/μs (1870 ft/s). A copper rather than fused quartz impactor was used to achieve a higher stress level in the test material. The magnitude of the unloading wave, however, was lower due to the higher impedance impactor. Three tests with sample thicknesses of approximately 10, 15, and 20 mm were completed. The profiles obtained in this series are displayed in Fig. 9.

The peak stress achieved in this series of tests was approximately 6.5 GPa. Initial loading was a sharp shock to about 0.16-0.19 km/s. There appeared to be some tendency for the amplitude of the initial shock to attenuate with propagation distance. Subsequent loading to the peak particle velocity level was characterized by a dispersive, finite duration, loading wave. The unloading wave traveled considerably faster than the loading wave, causing attenuation of the peak amplitude within the 10 mm propagation distance.

The stress-strain, stress-particle velocity and wave velocity data are plotted in Fig. 9. There is a significant decrease in slope of the loading stress-strain curve at about 2.5 GPa, and the hysteresis is quite large, a result which is indicative of the amount of energy dissipated in the material during passage of the finite amplitude stress pulse. The wave velocity-stress data are also very unusual and will be discussed more fully in a later section.

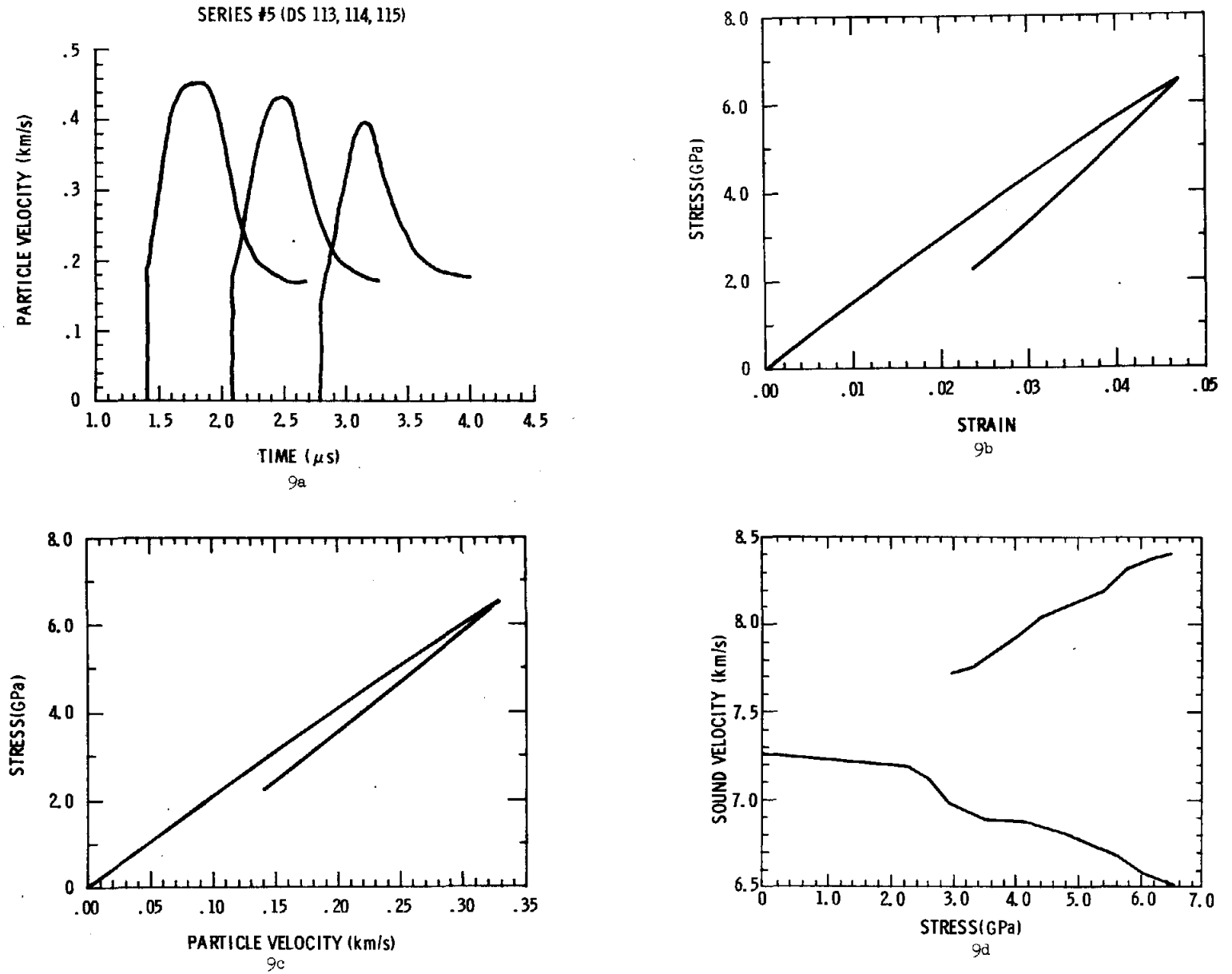

Fig. 9: WAVE PROFILES AND CONSTITUTIVE PROPERTIES FOR SERIES 5 TESTS.

Combined Results

In concluding this section, we present plots of the combined results for all five experimental series for the purpose of comparison and for later reference. In Fig. 10 the stress-strain curves and stress-particle velocity curves are shown. In Fig. 11 we show the same plots for the lowest three stress levels since they are obscured in the former plot. In Fig. 12 we show separately combined plots for the loading and unloading wave velocities.

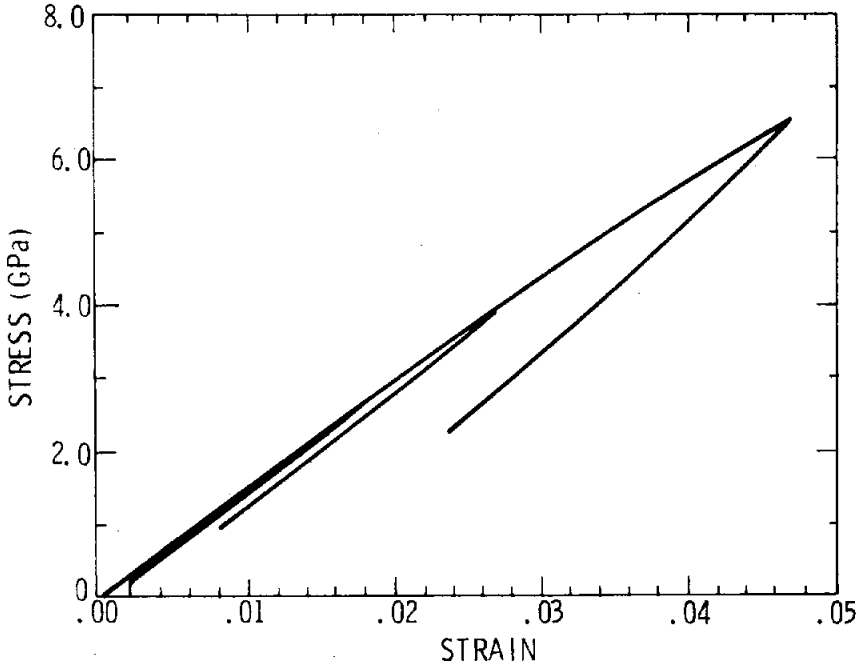

10a

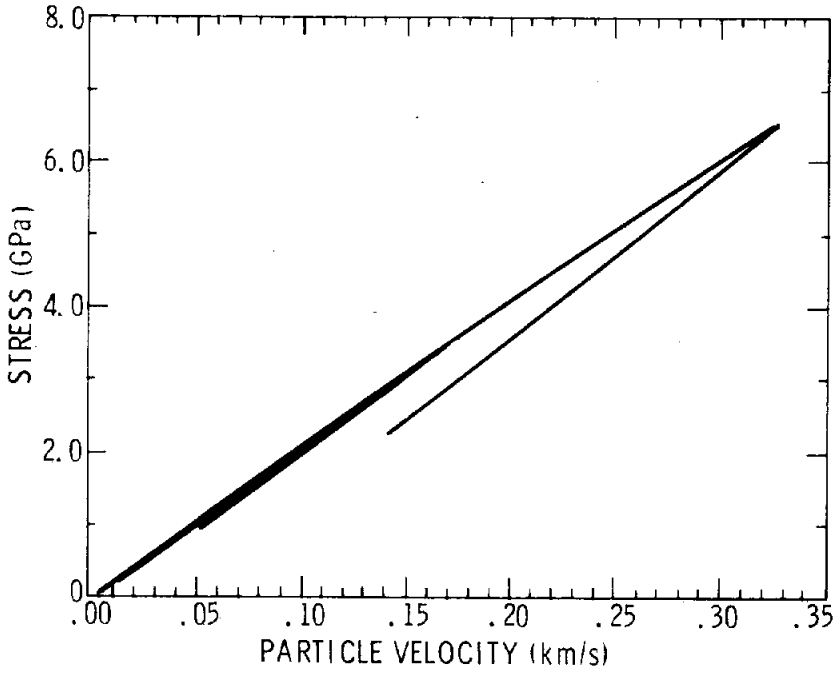

10b

Fig. 10: STRESS-STRAIN AND STRESS PARTICLE VELOCITY TO 6.5 GPa.

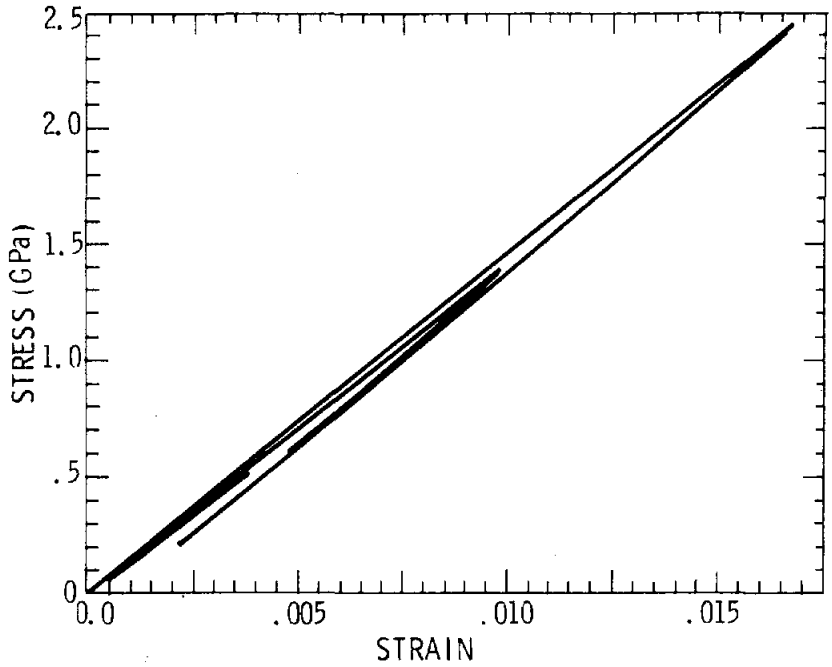

11a

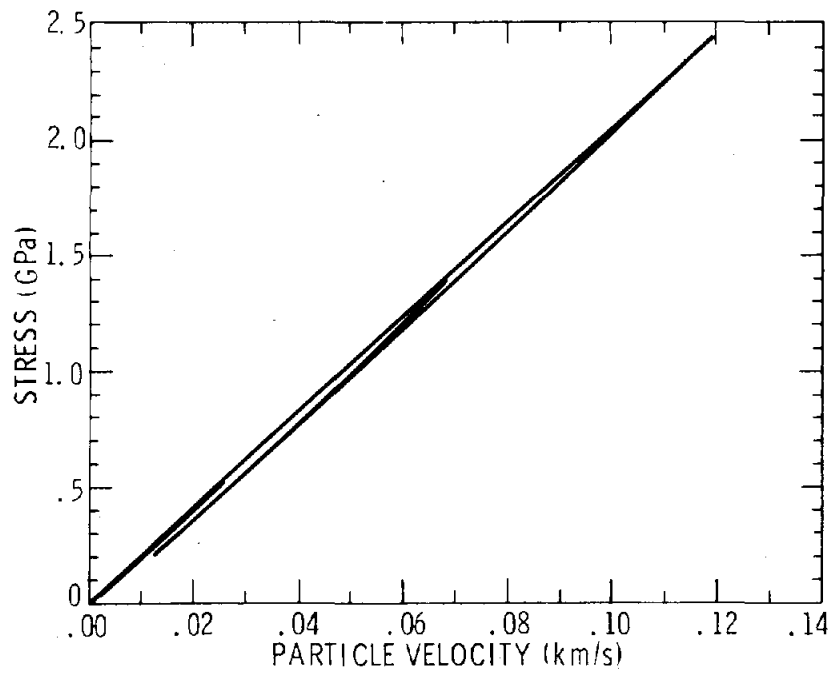

11b

Fig. 11: STRESS-STRAIN AND STRESS-PARTICLE VELOCITY TO 2.5 GPa.

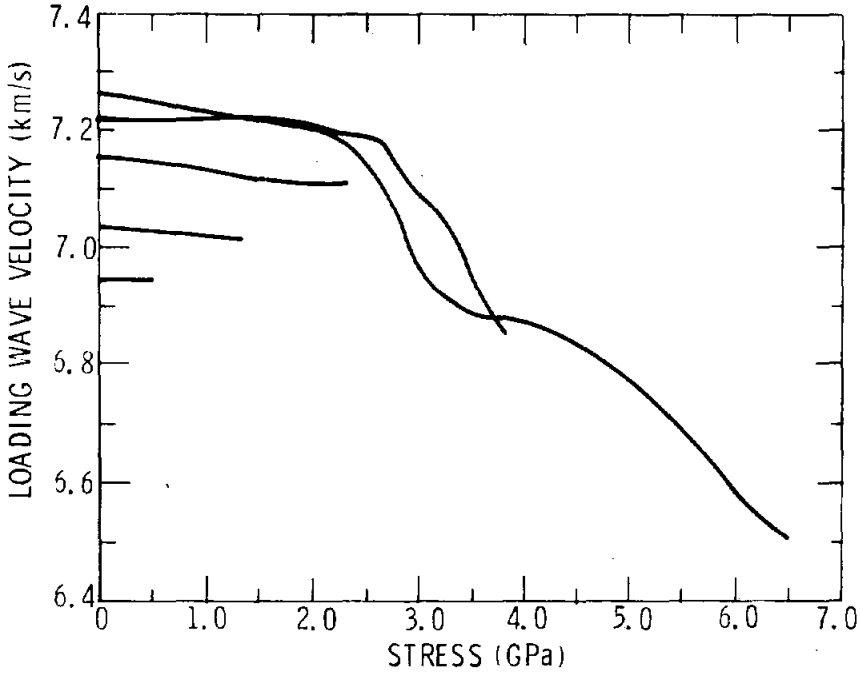

12a

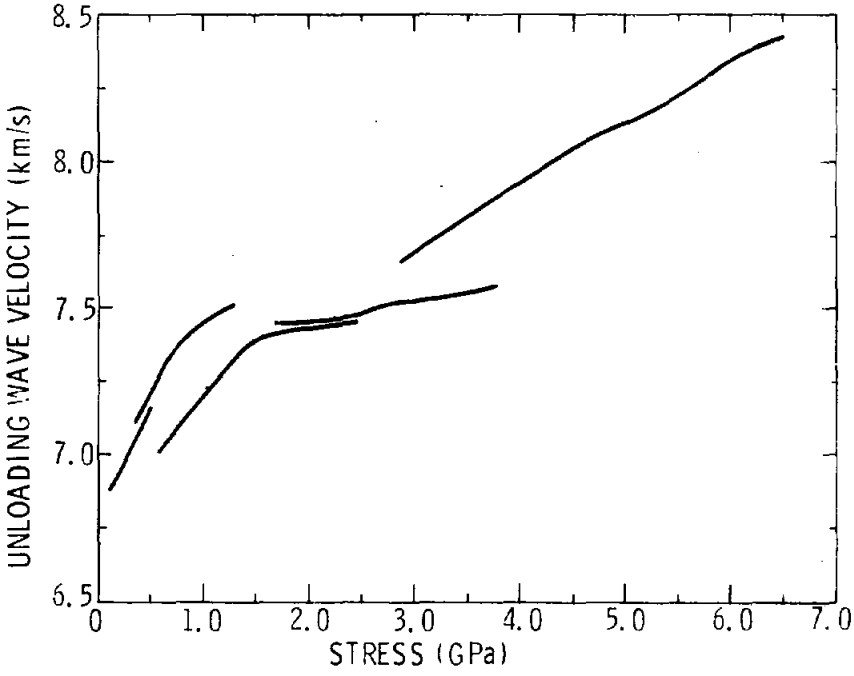

12b

Fig. 12: LOADING AND UNLOADING WAVE VELOCITIES IN BLAIR DOLOMITE.

V. DYNAMIC LOADING

The propagation velocity and dispersive character of the loading wave is determined by the mechanical properties of the rock material. Nonlinearity in the stress-strain curve is distinguished by changes in the wave velocity with increasing impact stress levels. Material yielding can usually be determined by a separation of the loading wave into several waves traveling at different velocities. When the separation of the waves is clearly defined, the stress level at wave separation is called the Hugoniot elastic limit* (HEL). Usually the onset of yielding is not abrupt and the loading wave behavior is more complex.

Earlier studies concerned with the onset of yielding in Blair dolomite have not left a clear picture. Petersen[3] reported an HEL of about 3.3 GPa but observed that the wave behavior was a shock followed by a rounded portion of the wave to peak stress. He concluded that an elastic wave equal to approximately one-half the driving stress was a good rule of thumb. Murri and Smith[6] in one experiment reported an HEL of about 3.0 GPa. Larson[4] in further shock wave studies at significantly lower stress levels also observed an initial shock followed by a gradual rise to peak stress.

In the present study we have identified two major, dramatically different, regions in the dynamic loading response of Blair dolomite. The first ranges from zero stress to 2.5 GPa. The second regime corresponds to stresses greater than 2.5 GPa. The difference can be seen in the profile character of the three series of tests below 2.5 GPa in contrast with

---

*The term Hugoniot elastic limit has a precise definition in terms of a yield stress after elastic loading in a shock wave experiment. We will relax the definition in the present context to include the stress at which large scale yielding initiates following elastic, viscoelastic, are possibly slight viscoplastic loading.

the two series above this stress level, in the first arrival velocity plot in Fig. 3, and most clearly, in the loading wave velocity plot shown in Fig. 12a. In Fig. 3, it is seen that the first arrival velocity increases with increasing driving stress to a level corresponding to a stress of about 2.5 GPa, after which no further increase in first arrival velocity is observed. The initial rise in velocity can probably be identified with increasing closure of preexisting cracks with increasing driving stress. Under a hydrostatic stress state, crack closure is usually observed to reach completion at a considerably lower stress level, however, Heard et al.[1] have observed that higher stresses are required to reach complete closure under uniaxial loading conditions.

In Fig. 12a the loading wave velocity as a function of stress amplitude for each series of tests has been plotted. Below 2.5 GPa there is a continued increase in velocity with increasing peak stress levels, and the wave velocity is essentially a constant function of the stress wave amplitude. For the two test series loaded to peak stresses in excess of 2.5 GPa the wave velocity is essentially constant to 2.5 GPa but shows a dramatic reduction above this stress level.

An important observation in the three series of profiles below 2.5 GPa was a snarp shock to a stress level well below the peak amplitude followed by a gradual rise over about 0.2 μs to the peak amplitude. Furthermore, the profiles below 2.5 GPa showed no change in profile structure with propagation distance indicating steady wave propagation.

In the experiments conducted at impact stresses greater than 2.5 GPa, dispersion is observed in the propagation character of the particle velocity profiles above 2.5 GPa. We suggest that material yielding occurs on loading at about this stress level and that the breaks observed in the

lower amplitude waves are not related to yielding. Strong evidence for this belief was inadvertently obtained from post-shot recovery of specimens. We were able to locate and identify substantial sized fragments (10-25 mm pieces) from all experiments conducted at peak stresses of 2.5 GPa or less. Only powder was recovered from the material shocked to higher stress levels.

The steady state, finite risetime wave propagation observed below 2.5 GPa implies that a rate dependent process is active during dynamic loading of the dolomite. The profile structure, a sharp shock followed by a gradual rise to peak amplitude, is strongly reminiscent of profile forms determined by Nunziato et al.[7] in a systematic study of finite linear viscoelasticity specialized to one dimensional wave propagation. This suggests that dolomite is exhibiting viscoelastic response below about 2.5 GPa.

VI. VISCOELASTIC RESPONSE

As was stated in the concluding remarks of the last section, we have observed steady state wave propagation in dolomite below a stress of about 2.5 GPa which strongly suggests a rate dependent process. Only a linear elastic or a rate dependent material model allow solutions of steady wave propagation with a finite risetime. A linear elastic model is inconsistent with the experimental conditions of a step loading input, which implies that the observed steady wave was required to evolve from this initial input condition. Rate dependence is the remaining explanation, and nonlinear viscoelasticity is consistent with the form of the observed profiles and the trend of the unloading stress-strain path, which suggests little or no permanent deformation.

Most compact crystalline rock with close to zero porosity have an abundance of small fissures and cracks. These small voids represent response of the rock due to tectonic stresses and relief of overburden during evolution of the rock species. They usually occur along grain boundaries as low aspect ratio cracks, and it has been observed that friction across crack surfaces generates hysteresis in an elastic load and unload cycle.[8] The degree of friction depends on the level of confining pressure as more of the initially open cracks are closed. This condition of sliding friction between crack faces should also occur during dynamic loading. Friction is usually identified as a rate independent process, although there are reasons to believe that under high rates of loading this may no longer be true. First, recall that a rate dependence of viscous forces in gases and liquids result from a transfer of mass between adjacent elements traveling at different velocities. Transfer of material between faces of metals during frictional sliding experiments have been observed and would contribute a

velocity dependence to the frictional force. Similar processes could occur in rock. Secondly, heat generated at the crack face due to friction has little time to diffuse in a dynamic experiment. Temperature rise will enhance plastic flow which in turn will effect the coefficient of friction. Temperature effects could also contribute to a rate dependent friction.

The wave profile data obtained from Series 1, 2, and 3 are sufficient to determine the model parameters for a finite linear viscoelastic model. The techniques required to fit viscoelastic models to steady wave profiles have been thoroughly explored by Nunziato et al.[7] and will be used here.

We have selected a differential expression for a generalized Maxwell material of the form

$$\frac{\partial \sigma}{\partial t} - E(\epsilon)\frac{\partial \epsilon}{\partial t} = -\frac{\sigma - \varphi_E(\epsilon)}{\tau} \tag{1}$$

to describe the viscoelastic response of the material. In conjunction with the equation of continuity

$$\frac{\partial \epsilon}{\partial t} + \frac{\partial u}{\partial h} = 0 \ , \tag{2}$$

and the equation of motion

$$\frac{\partial u}{\partial t} + \frac{1}{\rho_o}\frac{\partial \sigma}{\partial h} = 0 \ , \tag{3}$$

these equations constitute a complete system of hyperbolic differential equations which describe the evolution of one-dimensional waves in the medium. The Lagrangian space and time coordinates are h and t, respectively, and σ, ϵ, and u are the axial stress, axial strain, and material particle velocity, respectively. The function $\varphi_E(\epsilon)$ describes the equilibrium (quasistatic) stress-strain response of the material and $E(\epsilon)$ is a modulus associated with the instantaneous stress-strain response. τ is a single

time parameter which determines material relaxation in the intermediate time regime.

The instantaneous and equilibrium response curve are first determined from the data as is shown in Fig. 13. Since the profile is a steady wave the stress-particle velocity path follows a Rayleigh line and the Hugoniot jump conditions apply to a particle velocity level U_I which describes the instantaneous response and to a level U_E which describes the equilibrium response. The shock velocity-particle velocity data obtained from Series 1, 2, and 3 profiles are shown in Fig. 14, and were found to fit a linear shock velocity-particle velocity relation within experimental accuracy. The linear relation for the instantaneous response is

$$D = a_I + b_I u \tag{4}$$

and for equilibrium response is

$$D = a_E + b_E u \ . \tag{5}$$

Numerical values for the coefficients are provided in Fig. 14. Expressions for the equilibrium stress-strain response resulting from Eq. (5) and the Hugoniot jump conditions is

$$\varphi_E(\epsilon) = \frac{\rho_o \, a_E^2 \, \epsilon}{(1 - b_E \epsilon)^2} \ , \tag{6}$$

and for the instantaneous modulus is

$$E(\epsilon) = \rho_o \frac{a_I(1 + b_I \epsilon)}{(1 - b_I \epsilon)^3} \ . \tag{7}$$

The remaining parameter to fit in the viscoelastic model is the time constant τ. This is accomplished by assuming a steady wave solution and reducing the system of partial differential Eqs. 1, 2, and 3 to a single ordinary differential equation with the particle velocity u as the dependent variable.

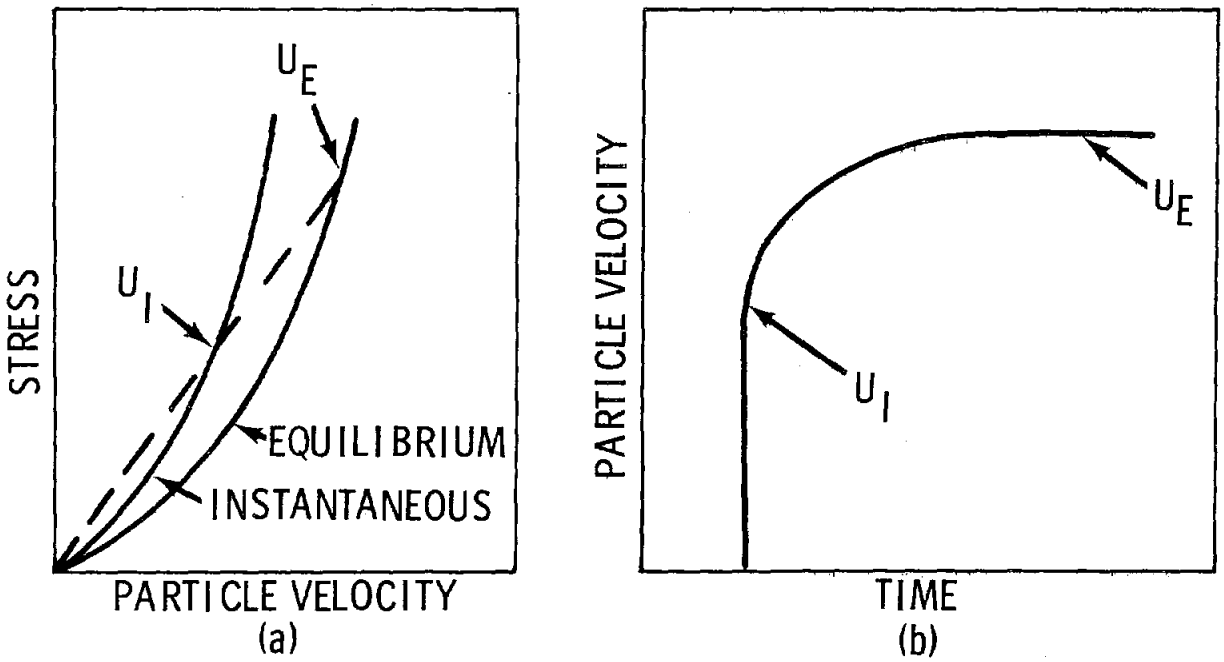

Fig. 13: VISCOELASTIC WAVE PROPAGATION.

In the loading path illustrated in (a) a steady particle velocity profile (b) consists of a sharp shock to an instantaneous value U_I followed by a gradual rise to an equilibrium value U_E.

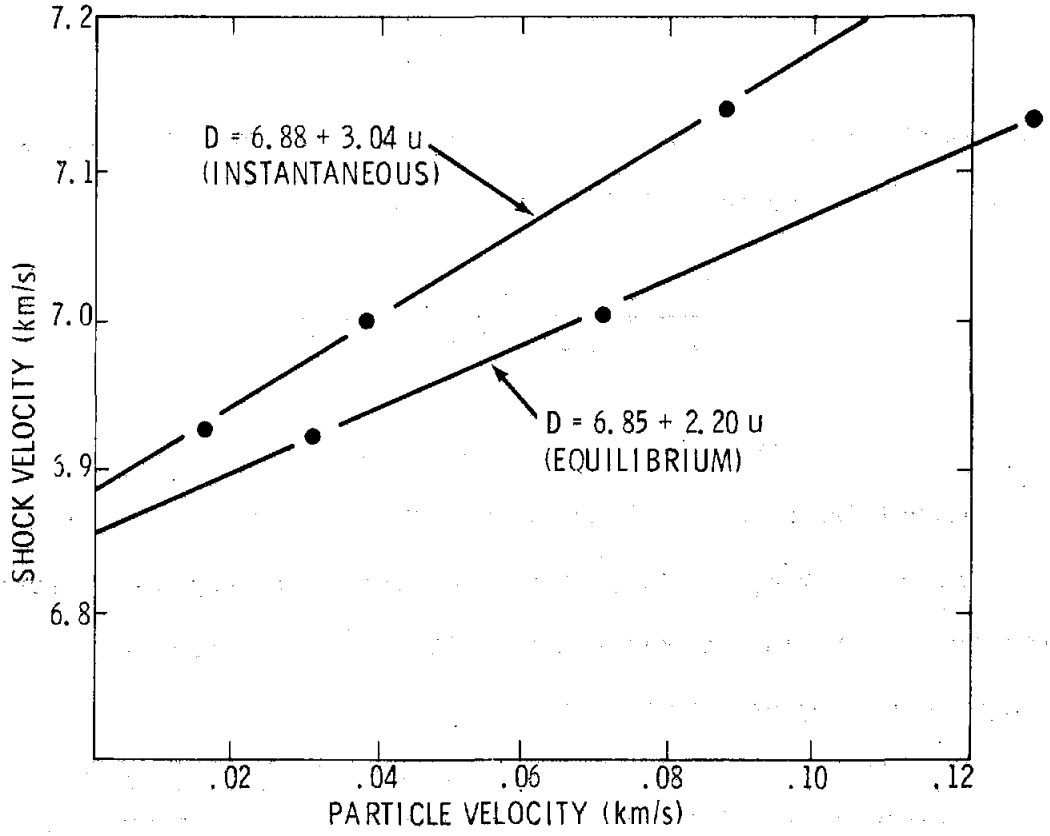

Fig. 14: INSTANTANEOUS AND EQUILIBRIUM SHOCK VELOCITY-PARTICLE VELOCITY CURVES (Stress ≤ 2.5 GPa).

The resulting differential equation can be integrated analytically to obtain a best fit to the experimental profiles.

The solution proceeds by assuming that stress, strain, and particle velocity are functions of the single dependent variable,

$$\zeta = t - \frac{h}{D} , \tag{8}$$

where D is the wave velocity of the steady profile. Equations 1, 2, and 3 then reduce to the ordinary differential equation

$$\frac{\rho_o D^2 - E(u)}{\rho_o D^2 u - D\varphi_E(u)} \frac{du}{d\zeta} = - \frac{1}{\tau} \tag{9}$$

where Eqs. 6 and 7 have been coupled with the Hugoniot relations to determine the functional dependence of E and φ_E on the particle velocity u. The expression $E(u) = \rho(a_I + 2\, b_I u)^2$ was used which is a very close approximation to the exact value in the particle velocity range of interest. The differential equation integrates to the expression

$$- \frac{\zeta}{\tau} = \alpha(u - u_I) + \beta\, \ell n \frac{u(1 - u/u_E)}{u_I(1 - u_I/u_E} + \frac{\gamma}{2}\, \ell n \frac{u_I(1 - u/u_E)}{u(1 - u_I/u_E)} \tag{10}$$

where

$$\alpha = 4\, b_I^2/D\, b_E$$

$$\beta = (2\, b_I/D\, b_E)[a_I + (b_I/b_E)(D - a_E)]$$

$$\gamma = -2(D^2 - a_I^2)/(D^2 - D\, a_E) + (4\, b_I/D\, b_E)[a_I + (b_I/b_E)(D - a_E)]$$

A best fit to the experimental profiles obtained in Series 1, 2, and 3 was obtained with a value of $\tau = 0.01\ \mu s$. The steady wave profiles determined from the model corresponding to the three series are shown in Fig. 15.

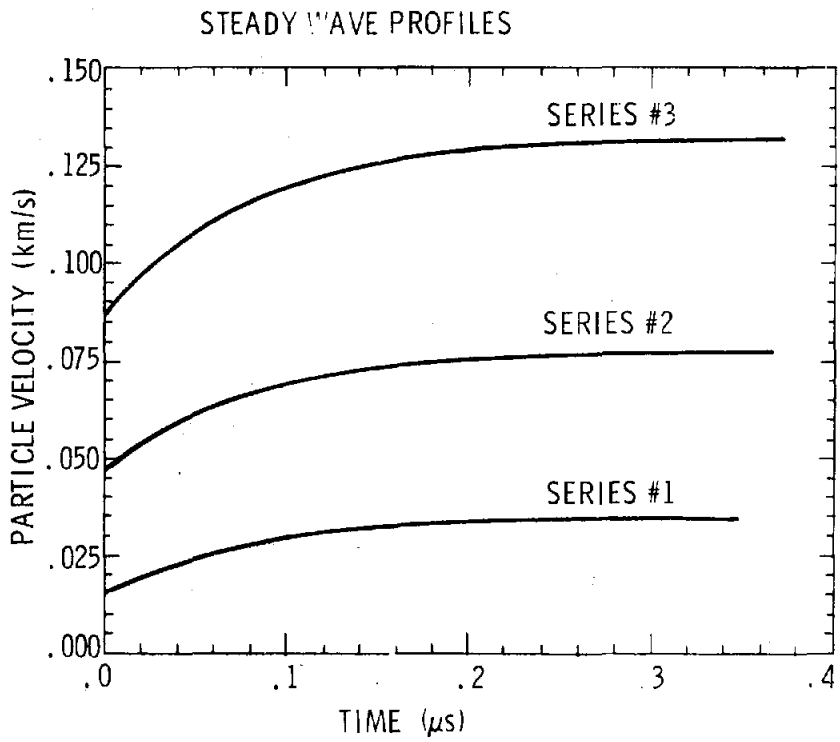

Fig. 15: LOADING PROFILES DETERMINED FROM FINITE LINEAR VISCOELASTIC MODEL FIT TO BLAIR DOLOMITE DATA.

The generalized Maxwell equation constitutive relation was found to adequately describe the loading wave propagation observed in Blair dolomite below 2.5 GPa. It remains to firmly identify the physical mechanism causing the rate dependent behavior. We have suggested rate dependent friction on closed cracks. It is possible, however, that a rate dependence associated with crack closure is responsible. Also, Barker[19] has shown that a Maxwell expression can result from dispersion effects in composite materials. At present we prefer friction since it is consistent with a possible explanation for the rate dependent yielding observed.

Schock and Heard[11] have compared the shock response and static properties in granite and have concluded that this material fails under shock loading by a process of brittle fracture. They have proposed that a slight break in slope in the initial loading wave observed in earlier shock wave studies corresponds to an onset of incipient microfracture in this material. We suggest that a rate dependent friction across closed cracks such as is proposed to explain the present data below 2.5 GPa, rather than fracture, as an alternative explanation for the wave propagation behavior observed in granite.

VII. DYNAMIC FAILURE (COMPARISON OF DYNAMIC AND STATIC RESPONSE)

We concluded in Section V that dolomite undergoes yielding at dynamic stress levels above about 2.5 GPa. This conclusion was based on the dramatic difference in dispersive character of the loading wave above 2.5 GPa which suggests the emergence of a second wave and the increased stress-strain hysteresis.

We will compare the 2.5 GPa dynamic yield stress with the static failure envelope determined for Blair dolomite by Handin et al.[9] and by Heard et al.[1] The comparison cannot be made directly since the transverse stress is difficult to measure in a plane shock wave experiment and cannot be inferred from the present experimental method. To compare dynamic yielding in the stress plane with the static failure surface, a reasonable assumption concerning the behavior of Poisson's ratio during the dynamic uniaxial loading is required. Walsh and Brace[8] have shown that cracks and voids in rock media undergoing uniaxial compression can significantly effect the magnitude of Poisson's ratio as closure occurs during compression. They differentiate between an effective Poisson's ratio descriptive of bulk behavior and an intrinsic Poisson's ratio characteristic of the matrix rock medium. As the cracks close with increasing compression and slip becomes prohibitive between crack surfaces, the effective Poisson's ratio approaches the intrinsic value. In static compression of Blair dolomite Heard et al.[1] observed values of Poisson's ratio equal to 0.22 at zero pressure, approaching a constant value of 0.34 above about 0.1 GPa.

Since, in the present comparison, we are interested in values of mean pressure to about 1.4 GPa, we chose to use a constant value of 0.34 to describe the dynamic loading behavior within the failure surface. This is

probably reasonably close to the intrinsic value of Poisson's ratio. The uniaxial loading path in shear stress-mean pressure space is then determined by the equation

$$\tau = \frac{3(1 - 2\nu)}{2(1 + \nu)} P \tag{11}$$

and is shown in Fig. 16. The longitudinal stress, $\sigma_y = 2.5$ GPa, is related to the shear stress and mean pressure through

$$P + \frac{4}{3} \tau = \sigma_y \tag{12}$$

which provides a second curve in Fig. 16 upon which the dynamic yield stress state must fall. Intersection of the curves determined by Eq. (11) and Eq. (12) provides an estimate of the dynamic yield state.

In Fig. 16 failure curves determined from triaxial compression experiments are shown.[1,9] Although the dynamic failure point falls somewhat beyond the range of the static curve, extrapolation suggests that the dynamic yield point is in reasonable agreement with the static failure surface.

Brace and Jones[10] have shown that the effect of strain rate ($\dot{\varepsilon}$) on failure is about 5 percent increase per ten-fold increase in $\dot{\varepsilon}$. The possibility of this strain rate effect occurring during shock loading has been discussed by Schock and Heard.[11] It is of interest to compare the present dynamic data with possible rate dependence of failure. In the present shock wave work, the yield strain of 0.017 was achieved by approximately linear loading in about 0.02 μs. The strain rate is, therefore, about 10^6 s^{-1}. Failure in the quasistatic tests of Heard et al.[1] was obtained at strain rates of 10^{-4} $^{-1}$. Assuming 5 percent per decade would suggest a 50 percent increase in the failure envelope. Since the loading path would have to intersect the dynamic failure curve at the

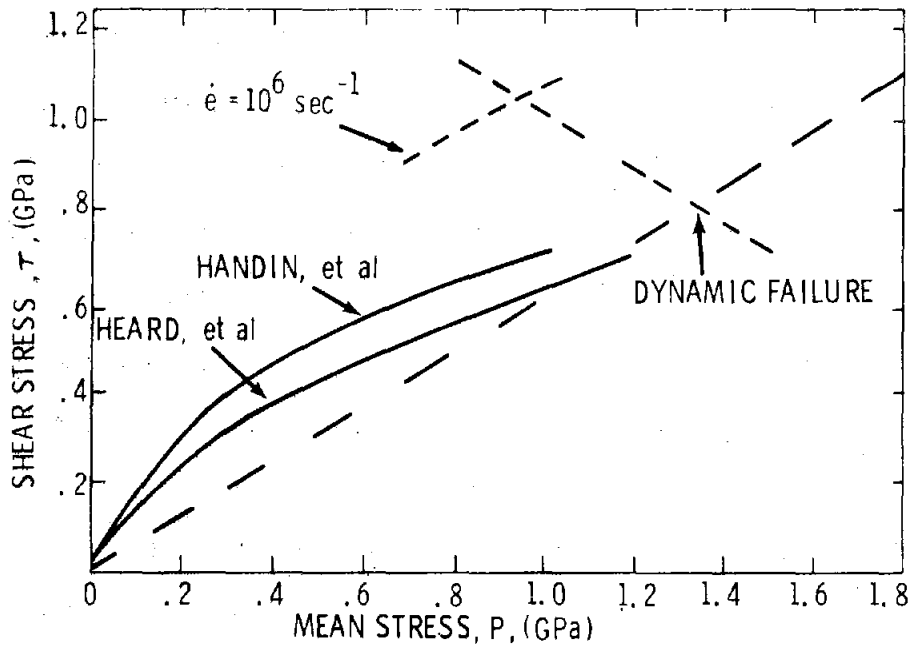

Fig. 16: COMPARISON OF DYNAMIC FAILURE STRESS AND STATIC FAILURE ENVELOPE FOR BLAIR DOLOMITE.

increased failure surface in Fig. 16, the value of Poisson's ratio implied can be calculated. A value of 0.08 was obtained which seems unreasonably low. We conclude that the shock data does not suggest a rate dependence of the failure envelope at the mean pressure achieved in dynamic uniaxial loading.

There remains to explain, then the dramatic discrepancy between the static uniaxial compression and the dynamic uniaxial compression data. In static uniaxial strain studies, it has been noted by several authors that rocks show significant departure from elastic behavior well before the failure envelope determined from triaxial compression tests is achieved. Brace et al.[12] have observed initiation of microfracturing and dilatancy at shear stresses of about one-half to two-thirds the failure value in uniaxial stress experiments. Schock and Heard[11] have attributed the departure from elastic behavior in uniaxial strain experiments to the stress state intersecting and remaining on the surface of dilatancy initiation during loading. Their argument is that a constraint of uniaxial strain precludes dilatant strain and, therefore, confining stresses will increase in such a manner as to limit the loading path to this surface of dilatancy. Although not strictly true (dilatant strain could occur at the sacrifice of more intense elastic strain), the basic argument seems reasonable and is in agreement with observed results.

It appears, referring to Fig. 1, that Blair dolomite under static uniaxial strain conditions yields at an axial stress of about 0.3 GPa. Under dynamic loading, yielding is suppressed until approximately 2.5 GPa is reached. To propose a possible explanation for this difference we will refer to the simplified illustration in Fig. 17. A material element aligned

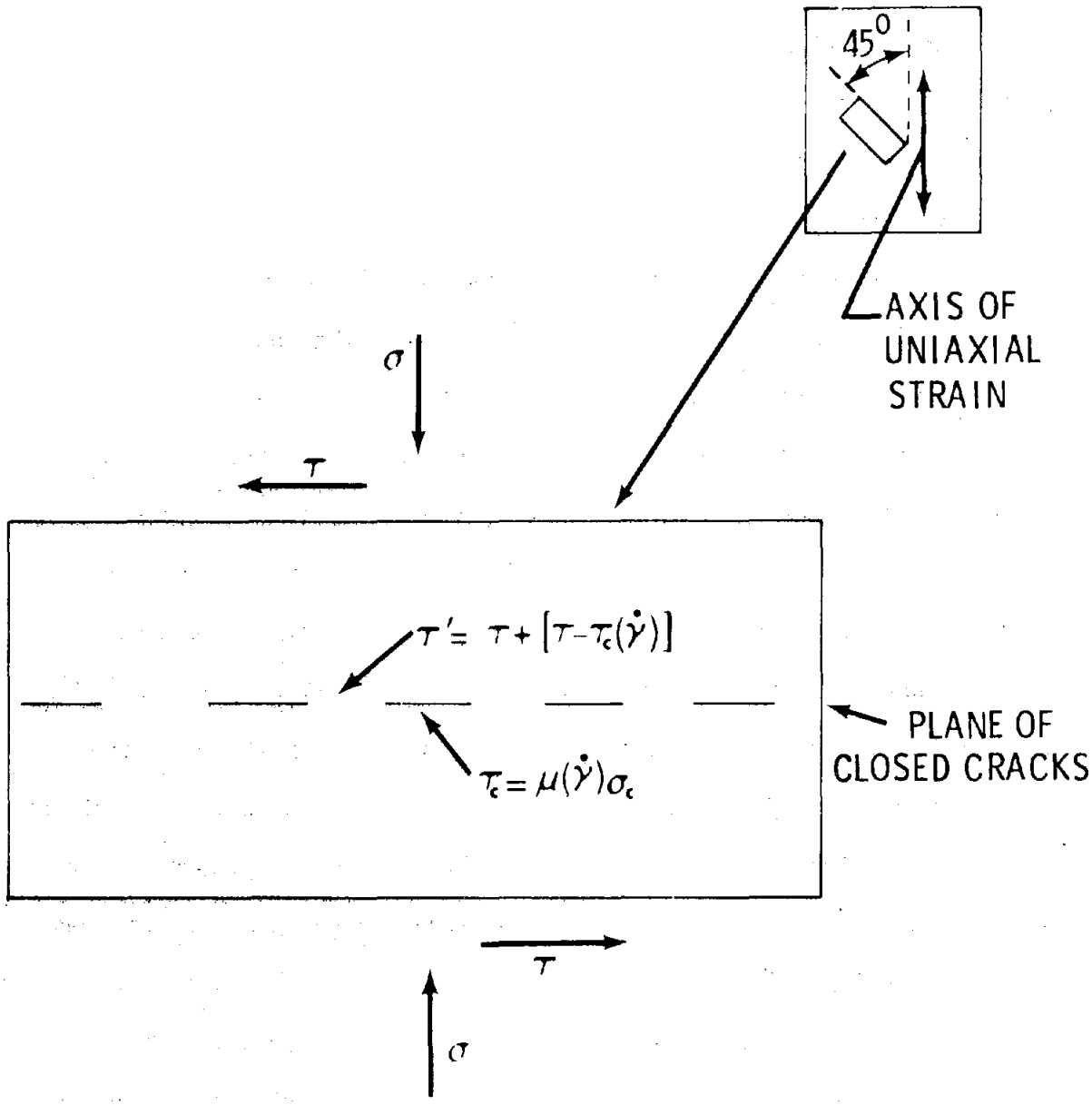

Fig. 17: RATE DEPENDENT SHEAR DURING DYNAMIC LOADING.

A material element oriented at 45° to axis of uniaxial strain. σ and τ are normal and shear stresses, respectively. Also shown is an idealized plane of closed cracks and the associated shear stress concentration at a shear strain rate of $\dot{\gamma}$.

at 45° from the axis of uniaxial strain is singled out such that the normal stress is $\sigma = (\sigma_1 + \sigma_2)/2$ and the shear stress is $\tau = (\sigma_1 - \sigma_2)/2$. We will consider a series of cracks aligned along a plane of shear. The cracks are closed due to the confining stress and, for simplicity, the crack area in this plane is equal to the area in which material integrity is maintained across the plane. Across the crack a normal stress σ_c less than, but on the order of σ, will be maintained. The shear stress transmitted across the crack due to the dynamic friction between surfaces will be $\tau_c = \mu(\dot{\gamma})\sigma_c$. We have shown functional dependence of the friction coefficient on shear strain rate due to the relative velocity between crack faces where we suggest that the coefficient of friction is strain rate sensitive. Since the total shear stress τ must be transmitted across this plane and since the sliding crack interfaces will support less than their share, stress concentrations must be supported by the regions of material integrity. To a first approximation, stresses in these regions will be intensified by a factor of $\tau - \tau_c(\dot{\gamma})$. At low strain rates τ_c is small and failure will occur early due to stress concentrations at areas of material integrity. At more rapid strain rates τ_c will increase, reducing stress concentrations and increasing the stress level at which failure occurs. Ultimately, at very rapid loading rates, material strength should approach that of the intrinsic strength of the matrix rock.

An axial yield stress of 2.5 GPa in Blair dolomite implies a resolved shear stress of about G/60 where G is the intrinsic shear modulus. If we recall that the maximum observed yield stresses achieved in single crystal whiskers approaches about G/15 to G/30, this strongly suggests that the

yield mechanism in dolomite under shock loading is intra-crystalline plasticity. Apparently, however, in the case of static loading fracture propagation is the dominant mode of failure. It would appear that there is a significant rate process involved in the yielding of dolomitic rock and, hence, a characteristic time constant corresponding to a transition from fracture, to intra-crystalline plasticity, as the dominant mode of inelastic deformation.

The difference in propagation characteristics of the loading wave is clearly evident in the loading wave velocity data shown in Fig. 12a. Concentrating on the two highest peak stress experiments, if elastic-perfectly plastic behavior occurred on loading, one expects an initial first wave velocity corresponding to the chord of the elastic Hugoniot followed by a slower second wave with a velocity corresponding to the slope of the plastic Hugoniot. The plastic Hugoniot should parallel the hydrostat and a shock velocity equal to the bulk sound speed at an intermediate level should be observed. Although there is an abrupt separation of waves at approximately 2.5 GPa (clearly seen in Fig. 9a), the second wave is dispersive. In fact, the wave velocity above 2.5 GPa, referring to Fig. 12, does not approach the expected bulk sound velocity value until the peak stress of 6.5 GPa is achieved on loading. The measured second wave velocity at 6.5 GPa is 6.5 km/s. This can be compared with the bulk sound velocity of 6.6 km/s at the same stress level which was estimated using a Murnaghan equation extrapolation[14] of acoustic data for Blair dolomite obtained by Heard et al.[1] and others.

We suggest two explanations which could account for the dispersive character of the second loading wave. First, at 2.5 GPa axial stress, the yield surface may still be an increasing function of mean confining

pressure. Second, after yielding, work hardening could expand the yield surface which would also account for the larger velocities observed. In fact, both effects probably come into play.

We must mention the fine structure observed in the loading wave velocity for the Series 5 experiments (6.5 GPa peak stress). The data suggests that at about 4.0 GPA a further increase in compressibility is achieved. We hesitate to dwell on this point since phase error or fringe timing error in the interferometer data could falsely introduce such a ripple. The data from Series 5 was excellent, however, and careful reanalysis of the data failed to uncover any problems.

Our only suggestion for a possible explanation is onset of a polymorphic phase transition at about 4.0 GPa. Such a transition has been inferred from high pressure Hugoniot data on dolomite[15] but the stress level at which the transition initiates has not been determined.

In Fig. 18 we compare the uniaxial stress strain paths for the two highest stress series with the hydrostat for Blair dolomite. The hydrostat to 3.6 GPa is that of Heard et al.[1] The hydrostat is extended to 7.0 GPa using a Murnaghan functional form and a pressure derivative of the bulk modulus of $dK/dP = 4.63$ estimated from acoustic data. We observed that in the dynamic shock wave tests significant material strength is retained in the material above the failure stress. Unloading proceeds by a single dispersive release wave. The behavior is not inconsistent with perfect elastic release. Since release was not measured to a level where the unloading path crosses the hydrostat and intersects the yield surface on the far side, it is not clear whether an elastic-plastic wave separation on unloading would occur.

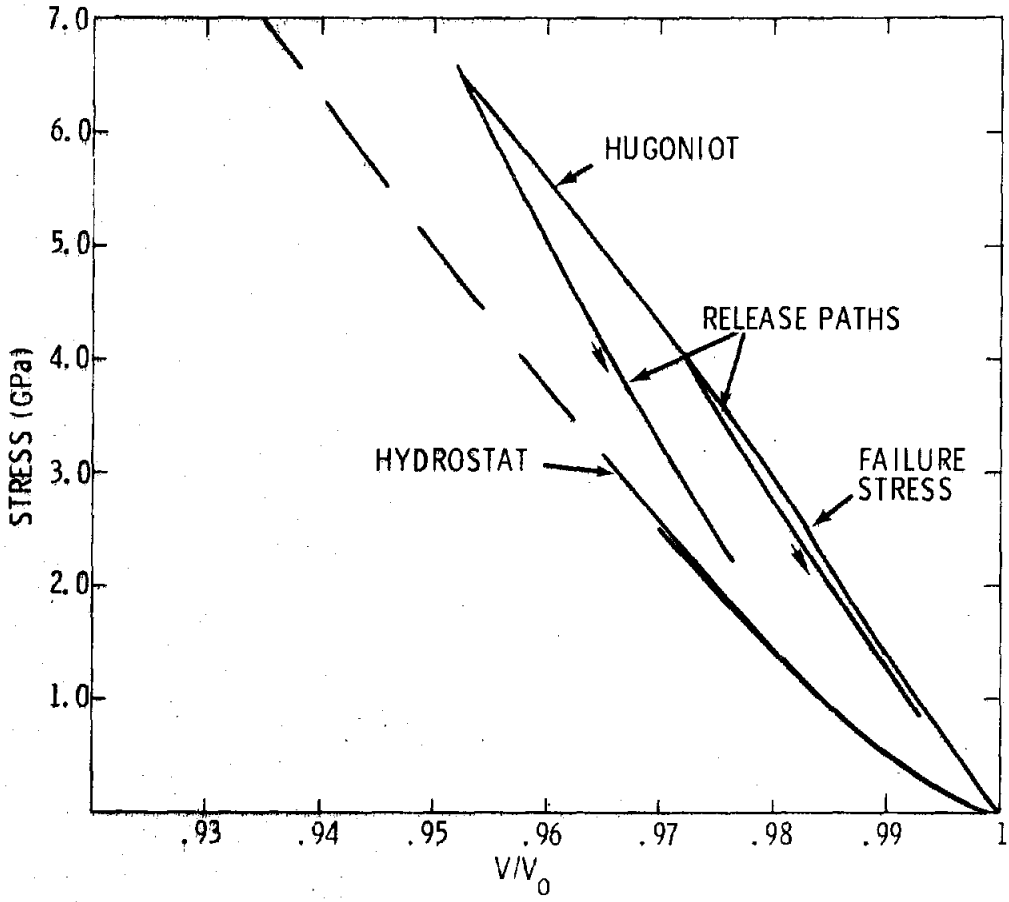

Fig. 18: COMPARISON OF HYDROSTAT AND DYNAMIC HUGONIOT AND RELEASE PATHS.

VIII. RELEASE WAVE BEHAVIOR

Referring to Fig. 12b, relief wave velocities for the experiments to peak stresses below 2.5 GPa were fairly constant down to a stress level of 1.0 to 1.5 GPa below which the release wave became more dispersive. Comparison of the relief wave velocity in Fig. 12b with the first wave arrival velocity in Fig. 3 shows a strong similarity. We have concluded that the behavior on relief is caused by the reopening of cracks which were elastically closed during the initial compressive wave. The reopening of cracks would re-introduce the softer effective modulus rather than the intrinsic modulus, consistent with the theory of Walsh and Brace[8], causing a reduction in the observed release wave velocity.

Above 2.5 GPA the relief wave is dispersive as is indicated by the continually decreasing release wave velocity with decreasing stress shown in Fig. 12b. In the Series 5 experiments, which reached a peak stress of approximately 6.5 GPa, the maximum relief wave velocity was sufficient to cause attenuation of the peak stress amplitude with propagation distance. Also, we noted a gradual rounding of the initial portion of the relief wave immediately behind the peak. This is in contrast to the more abrupt break in the relief wave arrival observed in the lower stress data and in similar studies on limestone. The gradual rounding is comparable to the relief wave properties observed by Barker and Hollenbach[16] in iron. Whether similar mechanisms are responsible is not clear.

As was suggested in the preceding section, if material behavior is elastic-plastic then the unloading velocity from about 6.5 GPa down to about 3.0 GPa should be characteristic of elastic response. A comparison can be made between the pressure dependence of the longitudinal modulus M determined from the shock release data and that determined from acoustic

data to 1.0 GPa. From the release wave data we obtain $dM/dP_m = 20$. This was determined using the wave velocity data in Fig. 12b between 3.0 and 6.5 GPa and the mean pressure determined from the extrapolated hydrostat in Fig. 18. This can be compared with a value of $dM/dP = 5.9$ determined from acoustic data. There are several possible explanations for the discrepancy: (1) although commonly assumed, the equivalence of the hydrostatic pressure P and the mean stress P_m which is used in the shock data where only one non-vanishing stretch occurs is not necessarily true. In a strict finite strain formalism the value of dM/dP can depend on the strain state achieved (hydrostatic or uniaxial). (2) The relief behavior may not be strictly elastic. (3) A portion of the dolomite may have transformed to a stiffer high density phase on loading causing the larger dM/dP on unloading. At this time explanation (1) seems the most reasonable.

IX. PETROGRAPHIC DESCRIPTION OF SHOCK-LOADED DOLOMITE

In section 5 it was noted that fairly substantial sized fragments (10-25 mm) were recovered from dolomite specimens shock-loaded to stresses as high as 2.5 GPa. The implication, of course, is that failure in dolomitic rock occurs at a stress level in excess of this value. The stress wave data, in fact, suggests a Hugoniot elastic limit at about this stress level. It is of interest to determine if the recovered samples bear any evidence of the shock loading and release wave process.

In this section we describe the general petrographic features of the shocked samples of the Blair dolomite. Although this rock is rather homogeneous, the predominance of very fine-grained matrix (0.02 mm in diameter, on the average) in these samples makes petrographic observations and fracture analysis quite difficult. It is considered likely that significant variations from the observations stated below may be present in other samples. Specimens were selected from each stress level experiment and thin sections cut parallel to the bedding plane (perpendicular to the axis of shock propagation) and perpendicular to the bedding plane (parallel to the axis of shock propagation) were prepared. Specimens will be identified by the peak shock stress and by parallel or perpendicular to the bedding plane.

<u>0.6 GPa (Parallel)</u>: Dolomitic, micritic limestone containing about 6% large (1-2 mm) dolomite crystals in a fine-grained, equidimensional matrix. Large crystals are twinned and are generally optically continuous. Grain boundaries are generally sharp. Fracturing is rare and no preferred fabric is demonstrated.

0.6 GPa (Perpendicular): Dolomitic, micritic limestone with well defined bedding fabric, generally marked by clay layers (clay = ~3% by volume of section), Large (~1 mm) crystals of dolomite are generally confined to the boundaries with clay layers and comprise about 10% of the volume of the section. Grain boundaries are well defined and sharp. Local curviplanar fractures are confined to grain boundaries and to the edge of the thin section; the fracture fabric is very weak to nonexistent and shows no distinct trend.

1.4 GPa (Parallel): Dolomitic, micritic limestone containing about 9% large (~1 mm) dolomite crystals in a fine-grained, clay-bearing (~4% by volume) matrix. Grain boundaries are locally poorly defined, both from microfracturing and recrystallization (?). Dolomite and matrix crystals show weak preferred elongation; twin planes do not demonstrate penetrative fabric. Fractures are common, both as en echelon cracks parallel to elongation fabric, and as radial and concentric fractures which radiate from, or encircle, respectively, the core axis. One en echelon fracture zone cross-cuts the elongation fabric and is about 0.8 mm wide. A true bearing for the elongation fabric cannot be established, since the sample is unoriented.

1.4 GPa (Perpendicular): Dolomitic, micritic limestone containing about 7% large (~1 mm) dolomite crystals interbedded with clay (~4%) and fine-grained micritic matrix. Large dolomite grains generally parallel bedding, are elongated along the bedding plane, and are generally concentrated along clay layers. Grain boundaries are somewhat indistinct from microfracturing and local recrystallization (?). Fractures are common and are primarily of two types: (1) parallel to bedding (possibly unloading

cracks), and (2) in a conjugate set oriented approximately 30° to the bedding plane.

2.5 GPa (Parallel): Dolomitic, micritic limestone containing about 8% large (1-3.5 mm) dolomite grains in a fine-grained, clayey (~3% by volume) matrix. Grain boundaries are indistinct and show microfracturing and recrystallization (?). Twins are present in the crystals and matrix but do not show penetrative fabric. Elongation fabric is not demonstrated. Radial and concentric fractures are present and are disposed as described in "1.4 GPa (Parallel)." En echelon fractures are also present but show no preferred orientation.

2.5 GPa (Parallel): Dolomitic, micritic limestone containing about 6% large (1-2 mm) dolomite crystals intercalated with somewhat faintly bedded clay (~4%) and matrix. Large dolomite grains with generally parallel bedding are somewhat elongated along the bedding direction. Grain boundaries are indistinct. Fractures include en echelon unloading (?) cracks parallel to bedding and a poorly defined conjugate set disposed as described in "1.4 GPa (Parallel)."

Results of the petrographic description are summarized in Table 2. Changes in grain size are apparently unimportant during shock loading of the Blair dolomite, since almost no variation in the amount or size of either dolomite crystals or matrix was observed in the shocked and unshocked samples. However, grain boundaries have presumably been microfractured during loading, and the intensity of this effect seemingly increases with increased load. Local recrystallization of carbonate along grain boundaries may be important, but this effect is outside the resolution of the petrographic microscope or cathode-luminescence techniques

used in this study. Elongation and twin fabrics are apparently of minor importance; however, the small size of the matrix, which makes up approximately 90% of this rock, makes detailed petrofabric analysis difficult.

The unshocked and 0.6 GPa samples showed no fracture fabrics, although minor fractures were locally observed. Samples shocked to 1.4 GPa and 2.5 GPa, however, contained well-defined, but generally non-penetrative fracture fabric. These fractures were disposed as radial, concentric, en echelon and conjugate fracture sets. Sections cut parallel to bedding, primarily display radial and concentric fracture sets which apparently radiate from, or encircle, the shock propagation axis. These fractures presumably reflect stress-release following shock loading of the sample perpendicular to the bedding plane.

Sections cut perpendicular to bedding show both fractures along bedding and conjugate fracture sets. Bedding fractures presumably reflect unloading (incipient spall) along the weak clay layers intercalated in the dolomite. The conjugate set is disposed with the obtuse angle of the set approximately bisected by the core axis. Apparently this set has been influenced by inhomogeneities in the rock particularly those of bedding, since in a general way one would expect the acute angle of the set to be bisected by the maximum compressional stress direction.

TABLE 2

Physical Properties of Shocked and Unshocked Blair Dolomite

Sample #	Crystal grain diameter, mm; average range in ( )	Matrix grain diameter, mm	Fractures	Comments
Unshocked (Parallel)	0.3-3.3 (0.3-1.0)	0.01-0.02	Minor; randomly oriented.	Equidimensional matrix grains; no preferred pattern of twins or grain-elongation; sharp grain boundaries.
0.6 GPa (Parallel)	0.3-1.7 (0.9-1.1)	0.01-0.03	No fractures observed.	Equidimensional matrix grains; no preferred fabric.
0.6 GPa (Perpendicular)	0.15-1.2 (0.4-0.6)	0.01-0.02	Minor; at edge of section.	Equidimensional grains; sharp grain boundaries; elongation of grains parallel to bedding.
1.4 GPa (Parallel)	0.15-1.8 (0.55-0.85)	0.005-0.02	Radial and concentric; local en echelon.	Grains show fractured edges; grain boundaries less distinct than DS-106; en echelon fracture zone 0.8 mm wide.
1.4 GPa (Perpendicular)	0.13-1.05 (0.55-0.80)	0.01-0.03	Common parallel to clay seams; also as conjugate set (see text).	Slight elongation of grains; large grains have long axes parallel to bedding; grains show fractured edges.
2.5 GPa (Parallel)	0.55-3.3* (0.95-1.8) *one large grain in sample	0.01-0.02	Radial and concentric; en echelon.	Grain boundaries commonly indistinct; large range in grain size (recrystallization effect?).
2.5 GPa (Perpendicular)	0.55-1.8 (0.8-1.2)	0.03-0.04	Frequent along bedding and clay seams; also as conjugate set.	Grain boundaries commonly indistinct and fractured; some elongation of grains parallel to bedding.

X. SUMMARY OF RESULTS AND CONCLUSIONS

1. A total of 13 plate impact experiments were completed on Blair dolomite in the stress range of 0.5 to 6.5 GPa. Diffuse surface velocity interferometry was used to determine stress wave propagation characteristics.
2. Wave propagation below 2.5 GPa exhibited a steady loading wave consisting of a sharp shock followed by a finite risetime of about 0.2 μsec to peak particle velocity. Unloading wave behavior indicated little, but not negligible, stress-strain hysteresis.
3. Wave propagation below 2.5 GPa is consistent in all respects with rate dependent finite linear viscoelastic behavior. A viscoelastic model was fit to the dolomite data below this stress level, and the model provided a satisfactory prediction of the loading wave behavior.
4. We speculate that rate dependent friction on preexisting closed cracks in the rock matrix is a physical basis for the observed rate dependent wave propagation.
5. Yielding occurs in Blair dolomite at an axial stress of approximately 2.5 GPa. This conclusion is inferred from the wave propagation characteristics for stress levels above 2.5 GPa which exhibit strong dispersion.
6. The 2.5 GPa axial failure stress is in reasonable agreement with the static compression failure envelope determined for Blair dolomite by other workers.
7. At lower stress levels static and dynamic uniaxial strain experiments differ dramatically (see Fig. 1). We speculate that in dynamic experiments, rate dependent friction increases supporting stresses across closed

crack interfaces inhibiting crack propagation and promoting intra-crystalline plasticity as the dominant mode of deformation.

8. Dynamic loading above the axial failure stress of 2.5 GPa maintains an approximately constant 1.5 GPa offset above the hydrostat indicating continued material strength and approximate elastic-plastic behavior. Unloading behavior is not inconsistent with elastic-plastic behavior

REFERENCES

1. Heard, H. C., A. Duba, A. E. Abey, and R. N. Schock, "Mechanical Properties of Blair Dolomite," Lawrence Livermore Laboratory, Rept. UCRL-51465 (1973).
2. Barker, L. M. and R. E. Hollenbach, "Laser Interferometer for Measuring High Velocities of any Reflecting Surface," J. Appl. Phys., Vol. 43, No. 11, September 1972.
3. Petersen, C. F., "Shock Wave Studies in Selected Rocks," Stanford Research Institute Rept. (1969).
4. Larson, D. B., H. C. Rodean, S. J. Spataro and J. R. Hearst, "ARPA-AEC Seismic Evasion Research Program Progress Report," Lawrence Livermore Laboratory, Rept. UCID-15948 (1971).
5. Barker, L. M., "Visar Data Reduction," Sandia Laboratories, Rept. SLA-73-1038 (1974).
6. Murri, W. J. and C. W. Smith, "Equation of State of Rocks," Stanford Research Institute, Rept. PGU 6618 (1970).
7. Nunziato, J. C., E. K. Walsh, K. W. Schuler and L. M. Barker, "Wave Propagation in Nonlinear Viscoelastic Solids," in Handbuch der Physik, Vol. VIa/4 (C. Truesdell, ed.) Springer-Verlag (1974).
8. Walsh, J. B. and W. F. Brace, "Elasticity of Rock in Uniaxial Strain," Int. J. Rock Mech. Min. Sci., 9, 7-15 (1972).
9. Handin, J., H. C. Heard, and J. N. Magouirk, "Effects of the Intermediate Principal Stress on the Failure of Limestone, Dolomite and Glass at Different Temperatures and Strain Rates," J. Geophys. Res., 72, 619, 1967.

10. Brace, W. F. and A. H. Jones, "Comparison of Uniaxial Deformation in Shock and Static Loading of Three Rocks," J. Geophys. Res., 76, 4913, 1971.

11. Schock, R. N., and H. C. Heard, "Static Mechanical Properties and Shock-Loading Response of Granite," J. Geophys. Res., 79, 1662, 1974.

12. Brace, W. F., and D. K. Riley, "Static Uniaxial Deformation of 15 Rocks to 30 Kilobars," Int. J. Rock Mech. Mining Sci., 9, 271, 1972.

13. Rice, J. R., "On the Stability of Dilatant Hardening for Saturated Rock Masses," J. Geophys. Res., 80, 1531, 1975.

14. Murri, W. J., D. E. Grady and K. D. Mahrer, "Equation of State of Rocks," Stanford Research Institute, Rept. PYU-1883 (1975).

15. Grady, D. E., W. J. Murri, and K. D. Mahrer, "Shock Compression of Dolomite," to be published in J. Geophys. Res.

16. Barker, L. M. and R. E. Hollenbach, "Shock Wave Studies of the $\alpha \rightleftarrows \varepsilon$ Phase Transition in Iron," J. Appl. Phys., 45, 4892 (1974).

17. Schuler, K. W. and D. E. Grady, "Compression Wave Studies in Solenhofen Limestone," in preparation.

18. Grady, D. E. and E. G. Young, "Evaluation of Constitutive Properties from Velocity Interferometer Data," Report 75-0650, Sandia Laboratories, Albuquerque, N.M. (1976).

19. Barker, L. M., "A Model for Stress Wave Propagation in Composite Materials," J. Composite Materials, 5, 140 (1971).

UNLIMITED DISTRIBUTION

DISTRIBUTION:
U.S. Energy Research and Development Administration
Bethesda Technical Library
Washington, D.C. 20545

U.S. Energy Research and Development Administration
ERDA Library
Washington, D.C. 20545

U.S. Energy Research and Development Administration
Albuquerque Operations Office
P.O. Box 5400
Albuquerque, NM 87115

D. K. Nowlin, Director
Special Programs Division
U.S. Energy Research and Development Administration
Albuquerque, NM 87115

T. J. Ahrens
California Institute of Technology
Pasadena, CA 91109

M. L. Barron
Paul Weidlinger & Associates
110 East 59th St.
New York, NY 10022

W. Brace
Massachusetts Inst. of Technology
Cambridge, MA 02139

J. F. Callender
University of New Mexico
Albuquerque, NM 87106 (5)

W. J. Carter, M-6
Los Alamos Scientific Laboratory
P.O. Box 1663
Los Alamos,NM 87544

R. J. Clifton
Dept. of Engineering
Brown University
Providence, RI 02912

D. R. Curran, G178
Stanford Research Institute
333 Ravenswood Avenue
Menlo Park, CA 94025

J. W. Dally
University of Maryland
College Park & Baltimore, MD 20740

G. Duvall
Dept. of Physics
Washington State University
Pullman, WA 99163

S. I. Green
Terra Tek, Inc.
420 Wakara Way
Salt Lake City, UT 84108

D. Grine
Systems, Science & Software, Inc.
P.O. Box 1620
La Jolla, CA 92037

J. Handin
Texas A&M University
College Station, TX 77843

H. C. Heard, L-437
Lawrence Livermore Laboratory
P.O. Box 808
Livermore, CA 94550

G. Jackson
USAE Waterways Experiment Station
P.O. Box 631
Vicksburg, MS 39180

J. N. Johnson
Terra Tek, Inc.
420 Wakara Way
Salt Lake City, UT 84108

D. Orphal
Physics International
2700 Merced
San Leandro, CA 94577

J. Ramsey
USERDA Fossil Energy
2100 M. Street N. W.
Washington, DC 20037

Distribution (cont.)

R. N. Schock, L-437
Lawrence Livermore Laboratory
P.O. Box 808
Livermore, CA 94550

L. Seaman
Stanford Research Institute
333 Ravenswood Avenue
Menlo Park, CA 94025

T. Stong, SPSS
Director, Defense Nuclear Agency
Washington, DC 20305

J. B. Walsh
Massachusetts Inst. of Technology
Cambridge, MA 02139

1325 W. J. Patterson
4363 W. E. Alzeimer
4363 D. L. McCoy
5000 A. Narath
Attn: 5200 E. H. Beckner
5400 A. W. Snyder
5700 J. H. Scott
5800 R. S. Claassen
5100 J. K. Galt
Attn: 5110 F. L. Vook
5120 G. J. Simmons
5130 G. A. Samara
5150 J. E. Schirber
5160 W. Herrmann
5162 L. D. Bertholf
5163 D. E. Munson
5163 D. E. Grady (15)
5163 R. E. Hollenbach
5163 K. W. Schuler (15)
5163 R. A. Schmidt
5163 E. G. Young
5163 W. R. Wawersik
5166 A. J. Chabai
5166 R. K. Byers
5167 B. M. Butcher
5167 J. R. Asay
5718 M. M. Newsom
5730 H. M. Stoller
5743 A. L. Stevens
8266 Tech. Library (2)
3141 Tech. Library (5)
3151 Tech. Writing (3)
For ERDA/TIC (Unlimited Release)
ERDA/TIC (25)
(3171-1 R. P. Campbell)